JVST A
Journal of Vacuum Science & Technology A
ARTICLE
pubs.aip.org/avs/jva

Reaction mechanism for HF based cryogenic plasma etching of SiO_2

Cite as: J. Vac. Sci. Technol. A **44**, 033006 (2026); doi: 10.1116/6.0005378
Submitted: 30 January 2026 · Accepted: 23 March 2026 ·
Published Online: 13 April 2026

View Online

Export Citation

CrossMark

Yeon Geun Yook,[1,a] Hyunjae Lee,[2,b] Sang Ki Nam,[3,c] and Mark J. Kushner[1,d]

AFFILIATIONS

[1]Electrical Engineering and Computer Science Department, University of Michigan, 1301 Beal Ave., Ann Arbor, Michigan 48109-2122
[2]Memory Manufacturing Technology Center, Samsung Electronics Co., Ltd., 1-1 Samsungjeonja-ro, Hwaseong-si, Gyeonggi-do 18448, Republic of Korea
[3]Non-residing Tech. Advisor, Samsung Electronics Co., Ltd., 1-1 Samsungjeonja-ro, Hwaseong-si, Gyeonggi-do 18448, South Korea

Note: This paper is part of the Special Topic Collection: Papers from the AVS 70th International Symposium.
[a]**Electronic mail:** ygyook@umich.edu
[b]**Electronic mail:** hj0928.lee@samsung.com
[c]**Electronic mail:** sangkinam@gmail.com
[d]**Author to whom correspondence should be addressed:** mjkush@umich.edu

13 April 2026 14:38:55

ABSTRACT

In semiconductor device fabrication, increasing the rate and quality of high aspect ratio (HAR) plasma etching is critical for the continuous scaling of three-dimensional (3D) devices. Cryogenic plasma etching (CPE) of SiO_2, in which the substrate is cooled to temperatures between −10 and −100 °C, is emerging as a promising approach for achieving high etch rates in HAR features. CPE of SiO_2 is typically performed in capacitively coupled plasmas (CCPs) with HF containing gas mixtures. The reaction between HF and SiO_2 generates H_2O, and its subsequent adsorption onto SiO_2 surfaces is believed to act as a catalyst that enhances the etch rate. The fundamental reaction mechanisms which account for the improved performance of CPE have not yet been clearly defined. In this paper, computational investigations of the surface kinetics in CPE of SiO_2 are performed for dual-frequency CCP reactors using $CF_4/H_2/Ar$ gas mixtures. Temperature-dependent mechanistic differences between cryogenic and room-temperature etching are analyzed through parametric variations of adsorption, condensation, etch yield, redeposition, implantation, specular reflection, and neutral transport. The mechanism is calibrated by comparing to experimental results (performed by others) for etch rates as a function of substrate temperature. The synergistic effects of these mechanisms on the etch rate and profile with respect to temperature are examined, along with the consequences of bias power.

Published under an exclusive license by the AVS. https://doi.org/10.1116/6.0005378

I. INTRODUCTION

The continuous scaling of semiconductor devices and the growing complexity of stacked architectures have motivated the development of advanced fabrication technologies and plasma based technologies in particular.[1,2] In this regard, device fabrication is increasingly reliant on plasma etching of high aspect ratio (HAR) structures.[3] (Aspect ratio, AR, is the height, or depth of a feature divided by its width.) Significant efforts have been devoted to overcoming defects that often occur in HAR plasma etching of vias, including bowing, profile distortion, twisting, mask selectivity, and charging effects.[4–7] The required attributes for devices, particularly in three-dimensional (3D) DRAM and 3D NAND having AR exceeding 100, are becoming extremely challenging for current plasma etching technologies to meet.[7,8]

One of the most critical challenges in HAR plasma etching is the aspect ratio dependent etching (ARDE) effect, also referred to as depth loading, in which the etch rate decreases as the AR increases during the plasma etching process. ARDE is thought to occur due to reduced fluxes and energies of ions and radicals to the etch front as AR increases, ultimately diminishing the etch yield and rate.[9–12] One method for reducing ARDE is to increase the bias power applied to the substrate, thereby increasing the incident

Published under an exclusive license by the AVS

ion energy and narrowing the angular distributions of ions (or hot neutrals) delivered to the etch front.[10] There is renewed focus on cryogenic plasma etching (CPE) as a method for enabling high etch rates and enhancing etch performance compared to conventional HAR etching.[13,14] CPE involves cooling the substrate to temperatures as low as −150 °C.

Although there is a renewed current focus on CPE, cryogenic etching was investigated as early as 1988, when Tachi *et al.* reported on anisotropic etching of Si using a microwave SF_6 plasma while cooling the substrate between −100 °C to −130 °C.[15] Subsequent studies on Si etching followed. In 1995, Bartha *et al.* reported that, even at −120 °C, isotropic etching of Si occurred in the absence of an O_2 passivation layer.[16] In 2005, Mellhaoui *et al.* demonstrated that inductively coupled plasma (ICP) SF_6 etching of Si at −110 °C remained isotropic without both bias power and an O_2 passivation layer. The process became anisotropic when the O_2 passivation layer was introduced, and bias power was applied.[17] In 2006, Tillocher *et al.* explained the anisotropic profiles at low temperatures through a model linking oxygen coverage with ion sputtering, showing that the oxygen proportion remained below the oxidation threshold at the etch front due to ion sputtering, while sidewalls became passivated with less ion bombardment.[18]

Research on CPE was initially conducted for the etching of Si. However, the current focus on CPE is on dielectric materials such as SiO_2 and Si_3N_4. Dussart *et al.* demonstrated the temperature dependence of CPE of SiO_2 and Si_3N_4 and the role of self-DC bias.[19] Research into the fundamental principles of CPE has shown that lowering the substrate temperature increases the sticking coefficient of etch precursors while reducing the rate of desorption, producing an enhanced physisorption layer on the substrate. Ion sputtering of the physisorbed layer then drives the etch reaction, which is generally recognized as the fundamental reaction mechanism in CPE.[20–25] For HAR structures, this implies that effective control of physisorption and efficient energy transfer via ion sputtering are key to optimizing performance.[21,26]

In general, industrial dielectric HAR etching of SiO_2 is performed using a dual-frequency capacitively coupled plasma (CCP) reactor, where the high frequency allows for plasma density control and the low frequency enables efficient ion acceleration. Conventional HAR etching of SiO_2 is typically performed with fluorocarbon-based plasmas.[27] While CPE of SiO_2 also primarily employs dual-frequency CCP reactors, its plasma chemistry has increasingly shifted toward hydrogen fluoride (HF) as the major etchant. Although anisotropic profiles have been achieved using fluorocarbon gas mixtures,[23,24] in HAR structures with relatively small critical dimensions (CDs), carbon-rich gas mixtures at low temperatures promote the formation of a heavy polymer layer due to increased physisorption resulting from the higher sticking coefficients. The thicker polymer layer leads to reduced etch rates. Consequently, recent dielectric HAR CPE processes have replaced carbon-rich fluorocarbons with carbon-lean gases such as CF_4 and NF_3, with HF emerging as the primary etchant.[13,14,28]

Hsiao *et al.* proposed that CPE of SiO_2 involves a pseudo-wet etching mechanism, where HF/H_2O adsorbed layers create an environment similar to conventional wet HF etching.[29] Experiments have confirmed the presence of H_2O on the SiO_2 surface during CPE, generated as an etch byproduct when ion sputtering acts on the adsorbed HF layer. At ambient temperature and pressures of tens of mTorr, volatile HF and H_2O remain in the gas phase rather than being adsorbed. However, at cryogenic temperatures, the increased physisorption rate enables a several nm thick adsorption layer.[21] The resulting H_2O adsorption facilitates an HF/H_2O vapor-phase etching environment for SiO_2, a mechanism extensively documented in the literature.[29–32] For example, Helms and Deal, Ono *et al.*, and Knotter concluded that the etching reaction is governed by HF hydrolysis and Si–O hydroxylation, both driven by adsorbed HF and H_2O.[30–32] In the context of CPE surface reactions, the adsorbed H_2O layer is thought to be essential for catalyzing HF hydrolysis and silanol group formation.

The benefits of CPE for dielectric materials include reduced bowing of the sidewalls of the feature, improved mask morphology, minimizing etch profile distortion, and mitigation of feature charge-up effects.[13,14,28,33] Among these, one of the most significant advantages of CPE is its higher etch rate and smaller ARDE.[28] While the exact causes of this etch rate enhancement are still under discussion, Lill *et al.* identified increased physisorption and enhanced neutral Knudsen transport and surface diffusion in the low-temperature environment as key contributing factors.[21]

In this paper, we discuss results from a computational investigation of the surface kinetics mechanisms for CPE of SiO_2. The work combines reactor-scale and feature-scale simulations of SiO_2 CPE in a CCP reactor using $CF_4/H_2/Ar$ gas mixtures over a temperature range from ambient to −110 °C. The primary etchant, HF, is generated through reactions between hydrogen and fluorine-containing species in the plasma, while H_2O is formed during etching through surface reactions of adsorbed HF catalyzed by ion bombardment. An overview of the CPE mechanism and descriptions of models are in Secs. II and III, respectively. Key surface kinetics mechanisms (including adsorption, condensation, etch yield, specular reflection, redeposition, ion implantation, and neutral transport) are discussed in Sec. IV, along with their effects on etch rates and profiles under cryogenic conditions. Finally, the overall temperature dependence of the etching mechanism is analyzed by integrating the individual subprocesses into a unified model to evaluate the synergistic effects of CPE. In Sec. V, the evolution of etch profiles, including bowing and tapering, is evaluated as a function of substrate temperature. Concluding remarks are in Sec. VI.

13 April 2026 14:38:55

II. OVERVIEW OF THE CRYOGENIC ETCH MECHANISM

While numerous reactions occur during the CPE process, the primary reaction flow can be summarized as

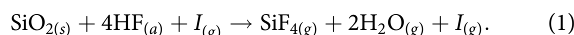

$$SiO_{2(s)} + 4HF_{(a)} + I_{(g)} \rightarrow SiF_{4(g)} + 2H_2O_{(g)} + I_{(g)}. \quad (1)$$

Here, the subscript (s) denotes the solid phase, (g) the gas phase, and (a) the adsorbed species on the surface. The symbol I represents any ion (or hot neutral) delivering activation energy. The incident ion is positively charged prior to surface impact. Upon impact, the ion is neutralized and becomes a hot neutral species, with the charge transferred to the surface. In this global reaction, 4 HF molecules reacting with SiO_2 remove Si as an SiF_4 etch product and O as H_2O. The reaction is accelerated by the

Published under an exclusive license by the AVS

activation energy provided by ion bombardment. In analogy to HF-wet etching of SiO_2, the process likely proceeds through the acid mechanism, which requires solvation of HF into water which is a product of the global reaction. The combination of evolution of water through the global reaction and enhanced adsorption rates at the low temperature provides a thin water layer (several nanometers) which facilities this hydration.

The sequence of events is sustained by gas-phase H_2O, generated from the etching reaction, which produces a condensed adsorption layer. Hydrolysis of HF then occurs in the H_2O adsorbed layer producing hydronium ions (H_3O^+) and the fluoride ion (F^- or HF_2^-),

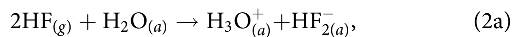

$$2HF_{(g)} + H_2O_{(a)} \rightarrow H_3O^+_{(a)} + HF^-_{2(a)}, \quad (2a)$$

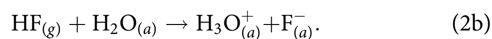

$$HF_{(g)} + H_2O_{(a)} \rightarrow H_3O^+_{(a)} + F^-_{(a)}. \quad (2b)$$

The hydronium contributes to the formation of silanol groups (Si–OH). Under ion bombardment, either direct or sequential reactions produce H_2O etch products, removing the oxygen and creating Si free radical sites ($Si\cdot_{(s)}$),

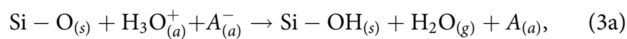

$$Si - O_{(s)} + H_3O^+_{(a)} + A^-_{(a)} \rightarrow Si - OH_{(s)} + H_2O_{(g)} + A_{(a)}, \quad (3a)$$

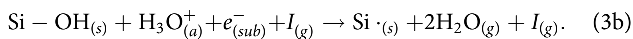

$$Si - OH_{(s)} + H_3O^+_{(a)} + e^-_{(sub)} + I_{(g)} \rightarrow Si\cdot_{(s)} + 2H_2O_{(g)} + I_{(g)}. \quad (3b)$$

Here, Si–O denotes a surface oxygen atom bound within the SiO_2 network (i.e., a bridging oxygen site), rather than a free SiO species. $A^-_{(a)}$ represents an anion (e.g., $F^-_{(a)}$ and $HF^-_{2(a)}$) that was formed during solvation of HF. The newly created $Si\cdot_{(s)}$ sites bond with fluoride ions, leading to the formation of SiF_n, which under ion bombardment leads to volatile etch products in the form of SiF_n,

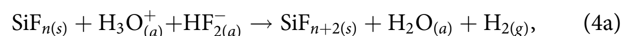

$$SiF_{n(s)} + H_3O^+_{(a)} + HF^-_{2(a)} \rightarrow SiF_{n+2(s)} + H_2O_{(a)} + H_{2(g)}, \quad (4a)$$

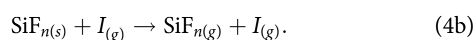

$$SiF_{n(s)} + I_{(g)} \rightarrow SiF_{n(g)} + I_{(g)}. \quad (4b)$$

The balance between the physisorption and desorption rates of H_2O determines the thickness of the condensed water later,

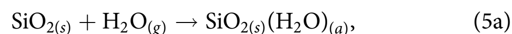

$$SiO_{2(s)} + H_2O_{(g)} \rightarrow SiO_{2(s)}(H_2O)_{(a)}, \quad (5a)$$

$$SiO_{2(s)}(H_2O)_n + H_2O_{(g)} \rightarrow SiO_{2(s)}(H_2O)_{n+1(a)}, \quad (5b)$$

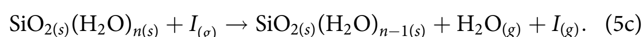

$$SiO_{2(s)}(H_2O)_{n(s)} + I_{(g)} \rightarrow SiO_{2(s)}(H_2O)_{n-1(s)} + H_2O_{(g)} + I_{(g)}. \quad (5c)$$

To activate the etch process, ions must penetrate through the condensed water layer. Increasing the thickness of the condensed layer reduces the penetration and energy of the ions reaching the etch front. In the CPE reaction mechanism, H_2O is both a catalytic component that facilitates the hydrolysis of HF and the formation of silanol groups, ultimately enhancing the etch rate, as well as a passivant whose condensed layer thickness can slow or terminate the etch process.[29–32]

III. DESCRIPTION OF THE MODELS

A. Reactor-scale model

The Hybrid Plasma Equipment Model (HPEM) was used to simulate a cylindrically symmetric CCP sustained in $CF_4/H_2/Ar$ gas mixtures. The HPEM is a two-dimensional (2D) computational framework intended for low pressure reactor scale simulations, as described in detail in Refs. 34–37. The HPEM comprises several modules, each addressing distinct physical phenomena and operating through an iterative, time-slicing process that achieves a cycle-averaged steady state. During this process, position- and phase-dependent quantities, such as densities, fluxes, and temperatures, are calculated and exchanged between modules. The modules employed in this work are the Fluid Kinetics-Poisson Module (FKPM), the Electron Energy Transport Module (EETM), the Plasma Chemistry Monte Carlo Module (PCMCM), and the Surface-Kinetics Module (SKM).

The FKPM is responsible for integrating the continuity, momentum, and energy equations for both charged and neutral species, alongside Poisson's equation to determine the electrostatic potential. This module provides densities, fluxes, temperatures, and electrical potential. The EETM receives these quantities and analyzes electron dynamics by resolving spatial and temporal electron energy distributions using a kinetic Monte Carlo approach. The EETM is executed for two classes of electrons: bulk electrons and secondary electrons emitted from surfaces and accelerated through the sheaths to high energies.[35] The spatially dependent electron energy distributions are used to produce rate and transport coefficients, and source functions that are used in the FKPM and PCMCM.

The PCMCM generates heavy particle energy and angular distributions (EADs) incident onto surfaces.[36] Using Monte Carlo methods, the PCMCM launches pseudoparticles throughout the reactor based on their source functions and integrates their trajectories until the particles are consumed, react to produce other species, or strike a surface during which time their EADs are recorded.

The SKM focuses on surface reactions, including etching, deposition, and passivation, at the plasma-surface boundary.[37] The SKM executes a surface site balance model using as input the fluxes of reactive species incident onto surfaces and computes site coverages for surface resident species, which produces reaction probabilities and deposition/etch rates. Based on these surface coverages, the SKM updates sticking coefficients and species returned to the plasma, which are then used by the FKPM.

A schematic of the cylindrically symmetric CCP reactor used in this investigation is shown in Fig. 1. The reactor consists of a 30 cm diameter substrate holding a Si wafer ($\varepsilon/\varepsilon_0 = 8$, $\sigma = 0.05$ S/cm) surrounded by a quartz ($\varepsilon/\varepsilon_0 = 4$) focus ring 6 cm wide. The top electrode, 36 cm in diameter, is separated from the wafer by a gap of 2.8 cm and surrounded by a quartz insulator. The sidewalls are grounded. The top electrode serves as a gas injecting showerhead with the annular pump surrounding the focus ring.

13 April 2026 14:38:55

Published under an exclusive license by the AVS

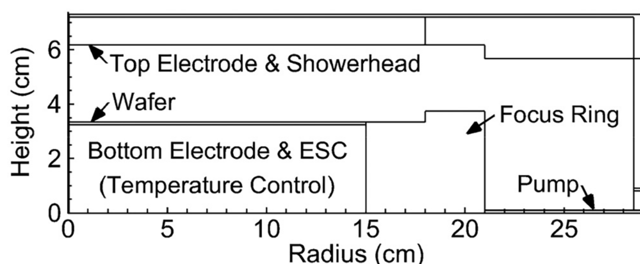

FIG. 1. Schematic of the cylindrically symmetric CCP reactor. The bottom electrode is connected to RF generators, blocking capacitors, and a chiller for controlling the substrate temperature in cryogenic etching.

Dual-frequency power at 40 and 2 MHz was applied to the substrate with the top electrode being grounded.

The temperature of the substrate electrostatic chuck (ESC), which is the powered electrode, is controlled and represents the wafer temperature. Generally, the wafer surface temperature is slightly higher than the temperature of the ESC setpoint because of heating from the plasma.[38] However, here we assume both to be at the same temperature. The base case has the substrate temperature (T_s) set to −60 °C, while the temperature of the walls including showerhead was set to 100 °C. Plasma conditions for the base case used a gas mixture of $CF_4/H_2/Ar = 15/15/70$ with a total flow rate of 300 SCCM. The pressure at the face of the pump was held at 30 mTorr. Dual-frequency sources were applied with a fixed source power of 1000 W at 40 MHz. The bias power at 2 MHz for the base case was 2500 W.

The reaction mechanisms employed for the $CF_4/H_2/Ar$ plasma have been discussed in the literature. Reactions involving fluorocarbon species and argon are described by Vasenkov *et al.*,[39,40] while hydrogen-related reactions are primarily based on the work of Volynets *et al.*[41] In addition, the reactions of HF, which is the most critical etchant species in this system, are comprehensively discussed by Manke and Hager.[42] The complete reaction mechanism consists of a total of 735 reactions. The rare gas species in the model include Ar, $Ar(4s[3/2]_2)$, $Ar(4s[3/2]_1)$, $Ar(4s'[1/2]_1)$, $Ar(4s'[1/2]_0)$, Ar(4P), Ar(4D), and Ar^+. Fluorine-containing species include F_2, F_2^*, F, F^*, F_2^+, F^+, and F^-. Hydrogen-related species include molecular hydrogen (H_2), with its ground and vibrationally excited states (v = 1–3), as well as H_2^*, H, H^*, H^+, and H_2^+. Hydrogen fluoride species include HF in the ground state, vibrationally excited HF (v = 1–3), and HF^+. Fluorocarbon species include CF_4, CF_3, CF_2, CF, C, CF_3^+, CF_2^+, CF^+, C^+, and CF_3^-. Etch by-products SiF_4, SiF_3, SiF_2, and H_2O are included to account for surface reactions.

Etch by-products are introduced into the bulk plasma through surface reactions at the SiO_2 wafer interface, here simulated by the SKM. These surface-generated species can subsequently participate in electron-impact reactions, dissociation processes, and other plasma-chemical pathways. Through the SKM, HF adsorbs onto the SiO_2 surface, forming a physisorbed layer. Under ion bombardment, the adsorbed HF layer etches the SiO_2 generating etch products SiF_x species and H_2O. A fraction of the generated H_2O desorbs from the surface, diffuses into the bulk plasma, and can return to the surface to participate in subsequent surface reactions, effectively acting as a reaction catalyst as discussed above. By employing the SKM, both the spatial distribution of H_2O in the bulk plasma and its flux toward the wafer surface can be quantified, enabling its direct utilization in feature-scale modeling and analysis. Representative plasma properties for the base case are shown in Fig. 2. To deliver 1000 W, the 40 MHz voltage amplitude is 473 V, and to deliver 2500 W, the 2 MHz voltage amplitude is 1640 V, with a self-DC bias of −823 V. The resulting sheath thickness is about 0.5 cm. The 40 MHz power sustains an electron density, which peaks at $8.1 \times 10^{10}\ cm^{-3}$ in the middle of the reactor. The electron-impact ionization rate by bulk electrons largely mirrors that of the electron density with a maximum value of $1.3 \times 10^{16}\ cm^{-3}\ s^{-1}$. The electron-impact ionization source by secondary electrons accelerated in the sheath is fairly uniform though it is maximum in the thick sheath where electrons are accelerated after emission.

The density of major ions, Ar^+, CF_3^+, and H_2^+ are shown in Fig. 2(b). Ar^+, CF_3^+, and H_2^+ are primarily generated by direct electron-impact ionization of their neutral parent species, including dissociative ionization for molecular precursors. Metastable-assisted ionization pathways (Penning ionization and metastable pooling) and charge exchange reactions provide supplementary pathways that contribute to the redistribution of the dominant ions in the plasma.

The neutral and ion fluxes incident on the wafer as a function of radius are shown in Fig. 3. The HF that sustains the etching reaction is produced by electron-impact dissociation of CF_4 producing F atoms, followed by H abstraction from H_2,

$$e + CF_{n(g)} \rightarrow CF_{n-1(g)} + F_{(g)} + e, \qquad (6)$$

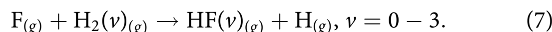

$$F_{(g)} + H_2(v)_{(g)} \rightarrow HF(v)_{(g)} + H_{(g)},\ v = 0 - 3. \qquad (7)$$

The abstraction reaction produces HF dominantly in vibrationally excited states. This reaction is favored by the high bond strength of HF and the low activation barrier of the abstraction process. Vibrational excitation of H_2 further enhances the reaction rate by effectively lowering the activation threshold, making this pathway a dominant source of HF. The total flux of HF(v) incident onto the wafer is $1.6 \times 10^{16}\ cm^{-2}\ s^{-1}$, the ratio of $v = 0/1/2/3$ is 0.49/0.28/0.16/0.06. The vibrational quanta of HF is approximately 0.5 eV (with excitation energies relative to $v = 0$ of 0.49, 0.96, 1.40 eV for $v = 1$–3, respectively),[43] resulting in a potentially significant flux of activation energy onto the wafer in terms of stored energy in vibrational modes of HF. The power flux of HF(v) delivered to the wafer is about $1\ mW/cm^2$. Although this is a small power density compared to the total power flux, the quantized energy brings with it the possibility of selectively activating surface processes. In this investigation, we did not distinguish between vibrational states of HF in the surface reaction mechanism. However, given the significant stored energy in HF(v), vibrational activation of surface processes should be a future consideration.

The neutral flux to the wafer is dominated by H atoms ($2.6 \times 10^{17}\ cm^{-2}\ s^{-1}$), which does not directly enter into our CPE

13 April 2026 14:38:55

Published under an exclusive license by the AVS

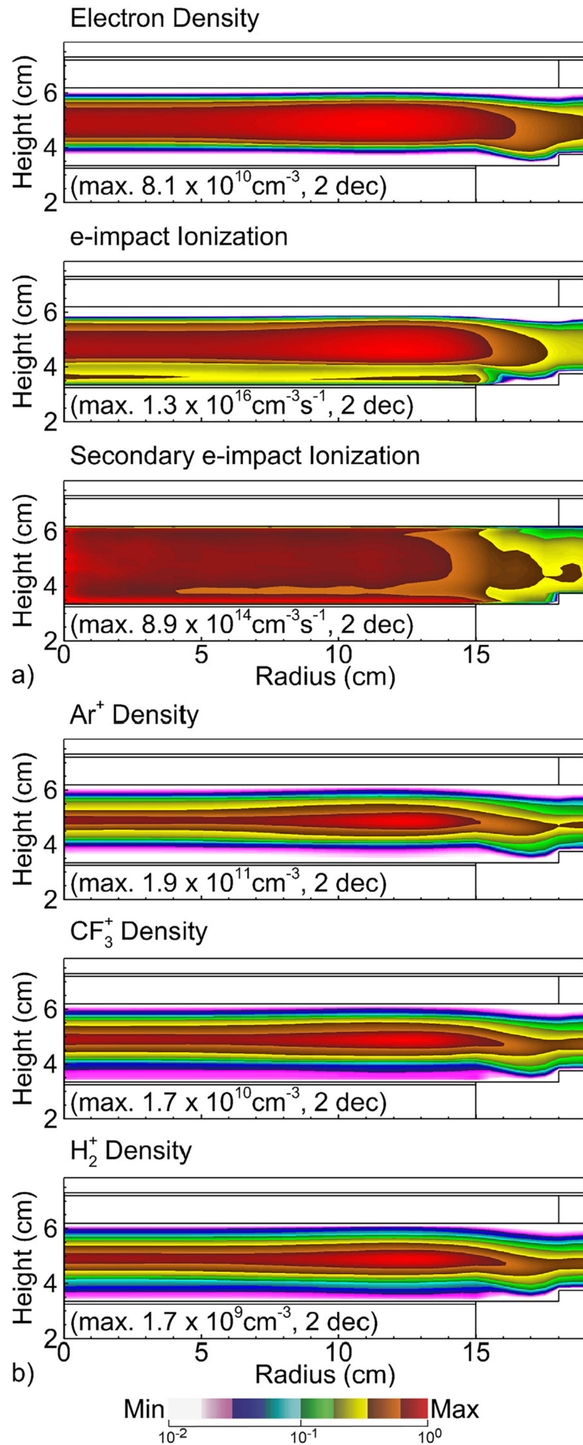

FIG. 2. Plasma properties at a bias power of 2500 W. (a) Electron density, electron-impact ionization source, and secondary electron-impact ionization source. (b) Densities of major ions. Images are a 2-decade log-scale with the maximum value indicated.

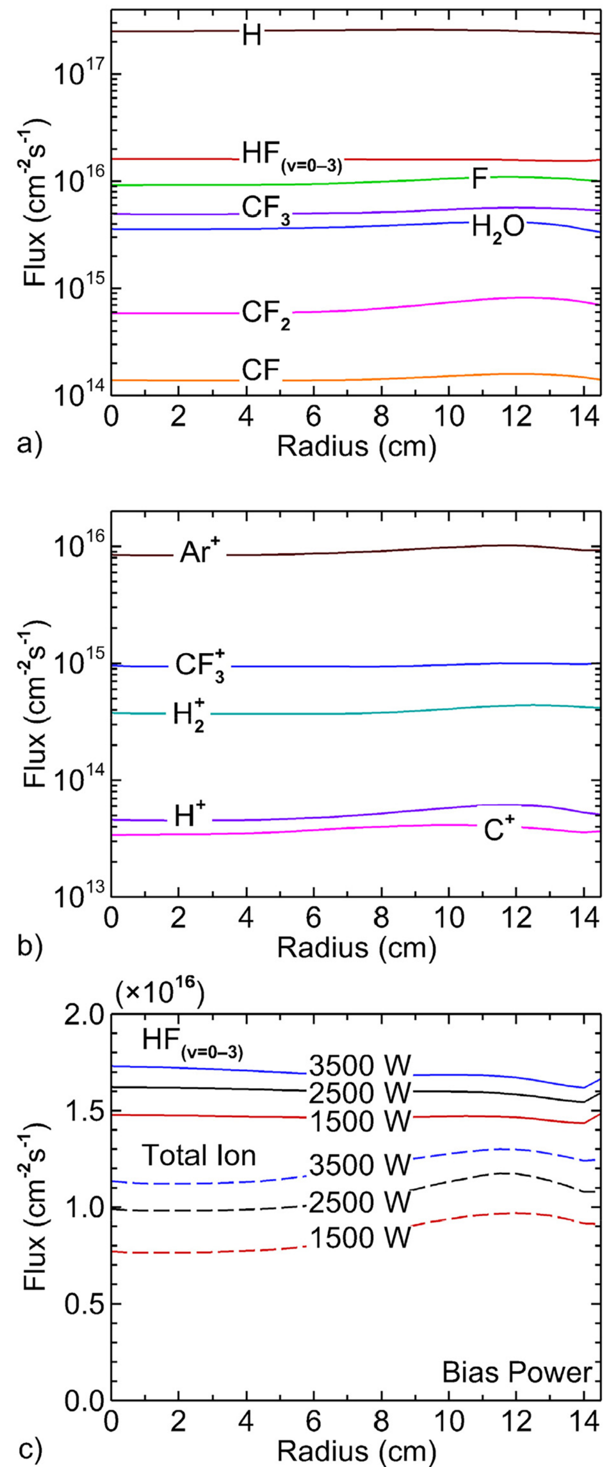

FIG. 3. Reactive fluxes to the wafer as a function of radius. (a) Neutral fluxes and (b) ion fluxes for bias power of 2500 W. (c) HF (vibrational states v = 0–3) and total ion fluxes at bias powers of 1500, 2500, and 3500 W.

13 April 2026 14:38:55

Published under an exclusive license by the AVS

surface reaction mechanisms. F (9.8×10^{15} cm^{-2} s^{-1}) and CF_3 (5.1×10^{15} cm^{-2} s^{-1}) have fluxes comparable to HF. F atoms participate in the CPE mechanism as a passivant of Si and CF_3 as polymer forming species.

H_2O is essential for silanol formation and HF hydrolysis as a catalyst of the etching process. Due to the lack of oxygen in the feedstock gases, H_2O is produced through surface reactions as an etch product. H_2O, which is not re-adsorbed within the features, enters the plasma with some likelihood of returning to the wafer as incident flux. Following the mechanism described for the SKM, the flux of H_2O returning to the wafer is 3.8×10^{15} cm^{-2} s^{-1}.

The ion fluxes incident onto the wafer are dominated by Ar^+ (9.0×10^{15} cm^{-2} s^{-1}) with secondary contributions from CF_3^+ (9.4×10^{14} cm^{-2} s^{-1}) and H_2^+ (3.7×10^{14} cm^{-2} s^{-1}). The dominant contributions of ions to the CPE mechanisms are activation of the etch and sputtering of the condensed water layer. The total ion fluxes and HF fluxes at the wafer surface for bias powers of 1500, 2500, and 3500 W are shown in Fig. 3(c). The bias power mainly affects ion energy, whereas radical and ion production via electron-impact reactions is primarily sustained by the 40 MHz source power. Therefore, the changes in fluxes of HF and ions are significantly less sensitive to bias power.

The ion energy and angular distributions (IEADs) summed for all ions are shown in Fig. 4 for bias powers of 1500–3500 W. For the base case of 2500 W, the amplitude of the 2 MHz voltage is 1640 V, the self-DC bias is −823 V, and the ion energies extend to approximately 2400 eV. With increasing bias power, the fraction of ions with higher energies increases with a narrower angular distribution. At 1500 W, the bias voltage amplitude is 1206 V, the self-DC bias is −695 V, and the incident ion energies into the wafer extend to about 1800 eV. At 3500 W, the amplitude is 1998V, the self-DC bias is −915 V, and the ion energies extend up to 2800 eV.

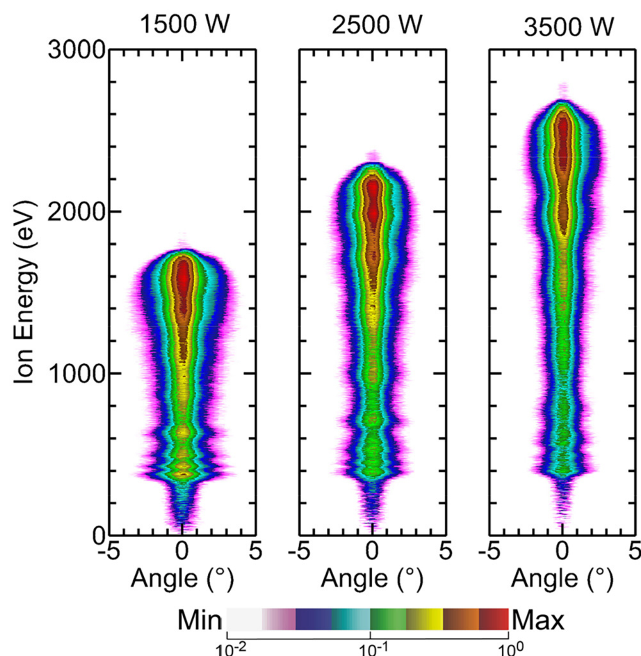

FIG. 4. IEADs at bias powers of 1500, 2500, and 3500 W for otherwise the base case conditions. The IEADs were plotted on a 2-decade logarithmic scale.

B. Feature-scale model and reaction mechanisms

The Monte Carlo Feature Profile Model (MCFPM) is a 3D voxel-based simulation used to predict the evolution of etch profiles in semiconductor materials.[44–46] Each voxel in the computational mesh represents a discrete solid material, and its identity changes based on surface reactions with incident fluxes such as etching, deposition, or passivation and by reactions with adjoining solid materials. The model uses pseudoparticles to represent gas-phase ions and neutrals, which are launched toward the surface with fluxes and EADs derived from the HPEM. The trajectories of these pseudoparticles are tracked until they interact with the surface, where a Monte Carlo-based mechanism determines the resulting reaction. Depending on the particle's energy and angle upon impact, the surface voxel may be removed, modified, or replaced by a new voxel. Reactions can also produce additional gas-phase particles, which are subsequently tracked until they are incorporated into the surface or leave the feature.

Although the SKM enables H_2O to be present in the bulk plasma at the reactor scale, using the SKM-predicted H_2O flux as a fixed input to the MCFPM does not capture the H_2O dynamics associated with ongoing etch reactions, including the resulting time-dependent variations in fluxes. To address this limitation, H_2O generation and consumption were modeled self-consistently within the MCFPM so that the transient behavior of H_2O is reflected during etching. At the start of the etch process, there is no flux of H_2O from the bulk plasma. Water is initially produced as a by-product of etching when ion bombardment interacts with the HF adsorption layer on the SiO_2 surface in the MCFPM. This gas-phase H_2O then transports within the feature. A portion of the H_2O re-adsorbs onto surfaces where it can participate in the etching reactions. The remaining H_2O exits the feature as out-flux into the bulk plasma. Subsequently, a fraction of the out-flux H_2O into the bulk plasma will return to the surface as an incident flux. The H_2O generation predicted by the SKM and the return flux of H_2O obtained from the HPEM were used as a guide to determine the magnitude of the H_2O leaving the feature that returns to the feature from the bulk plasma. During execution of the MCFPM, 10% of the H_2O leaving through the top boundary of the computational domain was returned to the feature as an isotropic flux of H_2O to represent this return flux.

The disposition of ions (or hot neutrals) reflecting from surfaces is important to both etch rate and profile control. In the model, ions (or hot neutrals) reflect from surfaces with specular and diffusive components that incorporate both incident angle and incident energy dependencies. In this investigation, we added substrate temperature dependence to the scattering coefficients as suggested by molecular dynamics simulations by Barsukov *et al.*[47] Across studies of scattering of ions from the surface, it has been observed that lowering the surface temperature reduces thermal lattice vibrations, leading to a narrower energy distribution of the

13 April 2026 14:38:55

Published under an exclusive license by the AVS

scattered particle and sharper scattering peaks.[48–50] As a result, ions undergo less energy exchange with the surface and retain more of their incident energy at lower temperatures. Under cryogenic etching conditions, the increased lattice rigidity enhances the specular component of ion (or hot neutral) scattering, enabling ions to retain a larger fraction of their incident energy.

Briefly, in the MCFPM, when ions scatter from surfaces, the reflected angle and reflected velocity are determined as follows:

$$\theta_r = \theta_i + \theta_t, \tag{8}$$

$$v_r = v_t + v_i \cdot f(\theta_i) \cdot f(E_i) \cdot s(T_s). \tag{9}$$

An ion striking a surface with incident energy E_i and angle θ_i with respect to the normal neutralizes and reflects as a hot neutral, which carries both thermal and specular components of scattering. (The same algorithms are used for an incident hot neutral.) In Eq. (8), the reflected angle, θ_r, is composed of a specular mirror reflection θ_i, plus a thermal deviation θ_t that accounts for surface roughness or thermal vibrations. The thermal deviation is modeled using either a Lambertian distribution ($\cos(\theta)$)[51] or a Phong distribution ($\cos^n\theta$, $n > 1$).[52] In Eq. (9), the reflected velocity, v_r, is determined by combining a thermal component with a specular component based on the incident velocity, v_i. The weighting functions $f(\theta_i)$ and $f(E_i)$ determine the fraction of incident energy retained in the reflected particle, so that grazing incidence and higher incident energy strengthen the specular component. For the base case, $f(\theta_i)$ increases from 0 to 1 between angles $\theta_i = 60°$ and 90°. $f(E_i)$ increases from 0 to 1 between energies $E_i = 100$ and 1000 eV. Although the model has the capability for unique weighting functions for different materials, these values were used for all materials. To account for temperature effects on specular scattering, $s(T_s)$, a temperature-dependent specularity factor was added to Eq. (10),

$$s(T_s) = 0.95 \cdot \exp(-0.003 \cdot (T_s - 203.15)), \tag{10}$$

where T_s(K) denotes the substrate temperature, $s(T_s)$ is designed such that lower substrate temperatures yield a larger specular component. The selection of this temperature dependence is discussed below.

The higher etch rates obtained with CPE compared to conventional processes likely require a higher yield. The etch yield is the number of atoms (or units of SiO_2) removed from the solid per incident ion (or hot atom/molecule). In this voxel-based model, each gas-phase pseudoparticle represents the same number of atoms as contained in a solid material voxel. Reactions that remove voxels from the solid are referred to as sputtering reactions. An etch yield of unity would remove a single voxel for an incident pseudoparticle. For etch yields less than or greater than unity, the following procedure is applied.

A gas-phase pseudoparticle strikes a solid voxel. Based on the incident energy and angle, the probabilities or yields for all inelastic reactions between the gas phase and solid species are computed. If the total probability or yield is less than 1, additional probability or yield allocated to elastic scattering is added to provide a unity probability or yield. If the total probability or yield is greater than 1, the inelastic probabilities are rescaled to sum to 1. A random number r [0,1] then determines which reaction occurs. If the reaction is a sputtering event, and its unscaled yield is less than 1, then the single voxel at the site of incidence of the gas-phase particle (the base voxel) is removed. If the unscaled yield is $n.x$ (n is an integer ≥1 and x is a fraction) then n voxels are first removed. If a random number r [0,1] $< x$, then an additional voxel is removed.

In the case of removing more than one voxel ($m > 1$), the base voxel is first removed. The nearest and next-nearest solid neighbors of the base voxel are then randomly selected. If the neighbor is an equivalent species, then voxel is removed with an appropriate etch product until $m - 1$ neighboring voxels are removed. An equivalent species is a material whose etch yield is at least equal to or greater than that for the base voxel for the energy and angle of incidence of the gas-phase particle. For example, if the base voxel is SiO_2 and neighboring voxel is Si having a larger yield, then Si would be an equivalent sputtering species to SiO_2. However, if the base voxel is Si and the neighboring voxel is SiO_2 having a smaller yield, then SiO_2 would not be an equivalent species to Si. For the high incident ion energies often encountered in HAR etching, this equivalent species criterion is perhaps overly conservative and will produce a lower limit on the yield.

Following this procedure, in a 3D cubic lattice, the maximum yield would be 27 (the total of the base voxel, nearest neighbors, and next-nearest neighbors). From a practical perspective, voxels located on a flat surface have at most 17 nearest and next-nearest neighbors. On a rough surface, the maximum nearest neighbors would be smaller.

When a pseudoparticle impacts the surface, implantation may occur. In this context, implantation refers to the penetration of the incident gas voxel into solid materials. The specific outcome of an incident particle reacting, reflecting or implanting when striking the surface is stochastically selected from a probability matrix depending on the surface material, incident energy and angle. A detailed description of the implantation model is in Huard *et al.*[46] Briefly, the penetration depth is stochastically sampled using the stopping ranges from Stopping and Range of Ions in Matter (SRIM),[53] and the projectile is advanced cell-by-cell while depositing energy and inducing local mixing via cell exchanges. After the projectile stops, an implantation site is formed by successive random displacements of neighboring cells, continuing until material is pushed to the surface or a prescribed displacement limit is reached based on the incident energy of the ion. Reactions occur between the implanted particle and voxels encountered during the trajectory and at its termination location.

MCFPM includes surface diffusion for physisorbed species. In the results discussed here, surface diffusion was included for physisorbed H_2O and HF. These species were allowed to diffuse over all surfaces except for the mask. After one of these species sticks to the surface in a physisorbed state, the pseudoparticle undergoes discrete hopping along the surface. The direction of hopping from the base voxel is randomly selected from the nearest and next-nearest neighbor voxels of the base location. If the surface on which the species has adsorbed is on the list of allowed surfaces for diffusion, then neighboring voxels are randomly queried. If the neighboring voxel is empty (that is, a gas cell) and a nearest neighbor of that cell is a solid upon which diffusion is allowed, the physisorbed

13 April 2026 14:38:55

Published under an exclusive license by the AVS

species hops to that site. If the site does not meet these criteria, another nearest neighbor site is chosen. If none of the nearest neighbor sites qualify, the physisorbed species is then immobilized. This process is repeated for a specified number of moves, which in the base case was 3000, after which the species is immobilized. At this point, the surface upon which the physisorbed species is in contact is examined for possible chemisorption reactions. If such reactions are allowed, one of the allowed reactions is randomly chosen based on its reaction probability. If no chemisorption reactions are allowed, the species retains its identity but is no longer allowed to diffuse.

An overview of the reaction mechanisms for the CPE of SiO_2 is in Table I. The complete reaction mechanism is described and listed in the supplementary material. The mechanism considers the adsorption of H_2O/HF, silanol (Si–OH) formation, hydrolysis of HF (hydrofluoric acid, H_3O^+:F^-) with H_2O, surface diffusion of adsorbed H_2O/HF, and the formation of silanol and fluorinated Si complexes (SiO_2:H_3O^+:F^-). These surface species are removed by physical and chemical sputtering reactions. Ion penetration through overlying water and acid adsorption layers activates the etch processes at the underlying solid boundary. Redeposition of etch products and SiO_2 physical sputtering products are accounted for. Ions neutralize when striking surfaces and reflect as hot neutrals, which undergo the same reactions with the same energy dependence as the original ions. Sputtering products having the same identity as incident gas-phase species are treated the same as those incident species. The exception is the product of SiO_2 physical sputtering, which redeposits to produce a passivation layer. The SiO_2:H_3O^+:$F^-_{(s)}$ complex represents a surface species of silanol and fluorinated Si, formed through HF hydrolysis in the presence of H_2O and subsequent reactions with the SiO_2 surface. Similarly, $SiO_2H_2O_{(s)}$ is used to represent all possible silanol groups that can be generated from the reaction between SiO_2 and H_2O.

Reactions of fluorocarbon (CF_x) species are summarized in Table II. These reactions include CF_x adsorption on activated SiO_2 sites to form SiO_2–CF_x complexes, subsequent polymer/passivation formation, and fluorination reactions leading to SiF_x formation. Physical and chemical sputtering, including implantation through overlying polymer layers, proceeds as described in Huang *et al.*,[44] where there is a more detailed discussion for reaction mechanisms for fluorocarbon-plasma based etching of SiO_2.

Due to the current lack of quantitative, temperature-dependent reaction probabilities (e.g., adsorption, condensation, etch yield, and specular reflection), it is challenging to assign probabilities based on fundamental theories when changing the substrate temperature. Therefore, during model development, these probabilities were generally scaled with increasing and decreasing substrate temperature without directly assigning specific temperatures to reaction probabilities. However, these scalings reflect, as much as possible, the physical relationships between temperature and the underlying processes. For example, adsorption probabilities are generally believed to increase with decreasing temperature,[21,23] and we adopted this scaling. Once the general trends for the temperature dependence of individual processes were established, the final tuning of the mechanism was accomplished by comparing the model predictions with experiments,[13] and at that time assigning likely temperatures to the model results.

IV. KEY SURFACE KINETICS MECHANISMS FOR CRYOGENIC PLASMA ETCH

In this section, the major surface-kinetics mechanisms that affect the scaling of CPE with substrate temperature are discussed. These investigations were conducted in the context of HAR etching of vias, which now have aspect ratios (AR) that often exceed 100. These conditions make it highly challenging to overcome the decrease of etch rate as the AR increases during etching, resulting in ARDE.[8,9,11,12] One of the motivations for developing CPE processes for dielectric etch of HAR vias is that CPE produces a higher etch rate and less severe ARDE than conventional ambient temperature processes.[13,14]

The initial conditions for feature-scale modeling using the MCFPM are shown in Fig. 5(a). A HAR via-contact structure of SiO_2 was employed, featuring a SiO_2 stack height of 5.4 μm with a 1 μm amorphous carbon (AC) layer serving as the mask. The mask opening width is 100 nm, resulting in a maximum aspect ratio of approximately 64 when including the mask layer, and about 54 when considering only SiO_2. The numerical mesh has 60 cells in width and depth, and 1320 cells in height, producing cubic voxels having dimensions of 5 nm on a side. Although pulsed power is now regularly used in CPE, the results discussed here are for continuous etching for a fixed period of 600 s.

A typical outcome of the reaction mechanism discussed below is shown in Fig. 5(a) after 600 s etch time for the base-case conditions ($T_s = -70$°C). To enable a consistent comparison of etch rates across conditions, the profile in Fig. 5(a) is shown at a partial-etch state before reaching the stop layer. That is, we are not including here (and the results discussed below) an overetch, which is continuing to etch after the stop layer is reached. Overetching is typically used to straighten tapers in the profile. By not overetching, the intrinsic tapering of the process due to passivation is made more clear. The etch mechanism for the AC mask was calibrated to provide a 5–6:1 selectivity with respect to the underlying SiO_2 so that mask erosion would not have a major effect on the etch profile. Etch profiles at equal time intervals are shown in Fig. 5(b) comparing $T_s = -70$ °C and ambient conditions ($T_s = +30$ °C). The etch rate for $T_s = -70$ °C is 295 nm/min compared to ambient conditions having an etch rate of 83 nm/min, a factor of 3.6 larger.

In both cases, as etch depth increases (aspect ratio increases), the etch rate decreases, indicating an ARDE effect. However, ARDE is less severe at the lower temperature. For $T_s = -70$ °C, the ratio of etch rate in the low-aspect-ratio regime (AR = 0–12) to that in the high-aspect-ratio regime (AR = 21–33) is 1.97. At ambient temperatures, this ratio is 3.04. In the absence of ARDE, this ratio would be unity, whereas a larger ratio indicates more severe ARDE. As discussed below, the reduced ARDE sensitivity in CPE is partly attributed to the *in situ* generation of H_2O deep within the feature. This H_2O acts as a precursor for forming the acidified adsorption layer during the etch process. With there being less reliance on the precursor having to transport from the plasma deeply into the feature, large AR is less of an impediment.

In this section, several processes that influence CPE performance are discussed. The base case has T_s being nominally −70°C, with parametric studies performed by varying reaction probabilities for each process individually. This section addresses mechanisms

13 April 2026 14:38:55

Published under an exclusive license by the AVS

TABLE I. HF–H_2O related reaction mechanism for cryogenic etching of SiO_2 used in the MCFPM.

Species		
M	All solid surfaces	(g) Gas phase
$I^{+,h}$	Ion or hot neutral[a]	(s) Solid
P	Passivation layer by redeposition	(a) Adsorption

Reaction	Description
Adsorption of HF and SiO_2 binding	
$HF_{(g)} + M_{(s)} \rightarrow HF_{(a)} + M_{(s)}$	HF adsorbs on all solid surfaces.
$HF_{(g)} + SiO_{2(s)} \rightarrow SiO_2HF_{(s)}$	HF adsorbs as a first dry etch step.
Adsorption of H_2O and silanol formation	
$H_2O_{(g)} + M_{(s)} \rightarrow H_2O_{(a)} + M_{(s)}$	H_2O adsorbs on all solid surfaces.
$H_2O_{(g)} + SiO_{2(s)} \rightarrow SiO_2H_2O_{(s)}$	Silanol group, Si–$(OH)_n$ ($n = 1$–3).
HF hydrolysis and fluorination	
$HF_{(g)} + H_2O_{(a)} \rightarrow H_3O^+{:}F^-_{(a)}$	HF hydrolysis (hydrofluoric acid).
$HF_{(a)} + H_2O_{(g)} \rightarrow H_3O^+{:}F^-_{(a)}$	
$HF_{(g)} + SiO_2H_2O_{(s)} \rightarrow SiO_2{:}H_3O^+{:}F^-_{(s)}$	Fluorinated silanol species comprising Si–OH and Si–F groups.
$H_3O^+{:}F^-_{(a)} + SiO_{2(s)} \rightarrow SiO_2{:}H_3O^+{:}F^-_{(s)}$	
H_2O condensation	
$H_2O_{(a)} + H_2O_{(g)} \rightarrow H_2O_{(a)} + H_2O_{(a)}$	Multiple layers of $H_2O_{(a)}$
Redeposition of $SiO_{2(g)}$	
$SiO_{2(g)} + M_{(s)} \rightarrow SiO_{2(s)} + M_{(s)}$	SiO_2 redeposits on all solid surfaces.
$SiO_{2(g)} + SiO_2{:}H_3O^+{:}F^-_{(s)} \rightarrow P_{(s)}$	Passivation layer from redeposition.
Physical sputtering	
$I^{+,h}_{(g)} + SiO_{2(s)} \rightarrow SiO_{2(g)} + I^h_{(g)}$	Physical sputtering of SiO_2.
Chemical sputtering	
$I^{+,h}_{(g)} + SiO_2HF_{(s)} \rightarrow SiF_{x(g)}$[b] $+ H_2O_{(g)} + I^h_{(g)}$	Sputtering of HF-binding sites.
$I^{+,h}_{(g)} + SiO_2H_2O_{(s)} \rightarrow SiO_{2(g)} + H_2O_{(g)} + I^h_{(g)}$	Sputtering of silanol sites.
$I^{+,h}_{(g)} + SiO_2{:}H_3O^+{:}F^-_{(s)} \rightarrow SiF_{x(g)}$[b] $+ H_2O_{(g)} + I^h_{(g)}$	Full sputtering of $SiO_2{:}H_3O^+{:}F^-_{(s)}$.
$I^{+,h}_{(g)} + SiO_2{:}H_3O^+{:}F^-_{(s)} \rightarrow SiF_{x(s)}$[b] $+ H_2O_{(g)} + I^h_{(g)}$	Partial sputtering of $SiO_2{:}H_3O^+{:}F^-_{(s)}$.
$I^{+,h}_{(g)} + SiF_{x(s)}$[b] $\rightarrow SiF_{x(g)}$[b] $+ I^h_{(g)}$	Sputtering of fluorinated Si.
$I^{+,h}_{(g)} + P_{(s)} \rightarrow SiF_{x(g)}$[b] $+ SiO_2H_2O_{(s)} + I^h_{(g)}$	Sputtering of passivation layer.
$I^{+,h}_{(g)} + H_2O_{(a)} \rightarrow H_2O_{(g)} + I^h_{(g)}$	Sputtering of condensation layer.
$I^{+,h}_{(g)} + H_3O^+{:}F^-_{(a)} \rightarrow H_2O_{(g)} + HF_{(g)} + I^h_{(g)}$	Sputtering of acid layer.
Surface diffusion of physisorbed layers	
$H_2O_{(a)} \rightarrow$ diff. $\rightarrow + SiO_{2(s)} \rightarrow SiO_2H_2O_{(s)}$	Surface diffusion of physisorbed H_2O and HF and their subsequent reactions of H_2O and HF with underlying surface.
$\rightarrow + SiO_2HF_{(s)} \rightarrow SiO_2{:}H_3O^+{:}F^-_{(s)}$	
$\rightarrow + H_2O_{(a)} \rightarrow H_2O_{(a)} + H_2O_{(a)}$	
$HF_{(a)} \rightarrow$ diff. $\rightarrow + SiO_{2(s)} \rightarrow SiO_2HF_{(s)}$	
$\rightarrow + SiO_2H_2O_{(s)} \rightarrow SiO_2{:}H_3O^+{:}F^-_{(s)}$	
Ion Implantation through adsorbed layers	
$I^{+,h}_{(g)} \rightarrow$ penetrate $H_2O_{(a)}$, $HF_{(a)}$ layers $\rightarrow + SiO_{2(s)}$, $SiO_2H_2O_{(s)}$, $SiO_2HF_{(s)}$, $SiO_2{:}H_3O^+{:}F^-_{(s)}$ $\rightarrow$ products	Energetic ions and hot neutrals penetrating adsorption layer and delivering energy to underlying surface.

[a]After collisions with surfaces, ions neutralize, and return as hot neutrals, which carry higher energy than thermal neutrals and can participate in the same reactions as ions.
[b]SiF_x denotes SiF, SiF_2, SiF_3, and SiF_4.

13 April 2026 14:38:55

Published under an exclusive license by the AVS

TABLE II. Fluorocarbon (CF_x) related reaction mechanism for cryogenic etching of SiO_2 used in the MCFPM.

Species		
M	All solid surfaces	(g) Gas phase
$I^{+,h}$	Ion or hot neutral	(s) Solid
Poly	Fluorocarbon polymer	(a) Adsorption

Reaction	Description
Adsorption of CF_x and SiO_2 binding[a,b]	
$CF_{x(g)} + SiO_{2(s)} \rightarrow SiO_2CF_{x(s)}$	CF_x adsorbs on activated sites
$CF_{x(g)} + SiO_2C_nF_{m(s)} \rightarrow SiO_2C_{n+1}F_{z(s)}$	to form SiO_2–CF_x complex.
Polymer deposition	
$CF_{x(g)} + M_{(s)} \rightarrow Poly_{(s)} + M_{(s)}$	Nonvolatile fluorocarbon polymer
$CF_{x(g)} + SiO_2C_nF_{m(s)} \rightarrow Poly_{(s)} + SiO_2C_nF_{m(s)}$	film (C–F rich deposit).
Fluorination	
$F_{x(g)} + SiF_{y(s)} \rightarrow SiF_{z(s)}$	Surface fluorination and volatile SiF_4 formation.
$F_{x(g)} + SiF_{y(s)} \rightarrow SiF_{4(g)}$	
$F_{x(g)} + SiO_2C_xF_{y(s)} \rightarrow SiFC_xF_{z(s)}$	
Chemical sputtering	
$I^{+,h}_{(g)} + SiO_2C_3F_{y(s)} \rightarrow SiO_2CF_{y(s)} + C_2F_{z(g)} + I^{h}_{(g)}$	Chemical sputtering of fluorocarbon-covered SiO_2.
$I^{+,h}_{(g)} + SiO_2C_2F_{x(s)} \rightarrow SiOCF_{x(s)} + CO_{(g)} + I^{h}_{(g)}$	
$I^{+,h}_{(g)} + SiO_2CF_{x(s)} \rightarrow SiF_{x(g)} + CO_{2(g)} + I^{h}_{(g)}$	
$I^{+,h}_{(g)} + SiOCF_{x(s)} \rightarrow SiF_{x(g)} + CO_{(g)} + I^{h}_{(g)}$	
$I^{+,h}_{(g)} + Poly_{(s)} \rightarrow Poly_{(g)} + I^{h}_{(g)}$	Polymer sputtering.
Ion Implantation through adsorbed layers	
$I^{+,h}_{(g)} \rightarrow$ penetrate adsorbed layers	Ion penetration through passivation layer enabling underlayer reactions.
$\rightarrow + SiO_{2(s)}, SiO_xC_yF_{z(s)} \rightarrow$ products	

[a] CF_x denotes CF_3, CF_2, and CF.
[b] F_x denotes F_2, and F.

13 April 2026 14:38:55

affecting etch rates, whereas profile analysis, such as bowing, is discussed in Sec. V.

A. Adsorption

As the surface temperature decreases, the dominant type of adsorption occurring within the etch feature is physisorption.[21] One of the most critical phenomena in CPE is the increase in adsorption probabilities with decreasing substrate temperature.[23] At cryogenic temperatures, the net adsorption probability of a molecule (or atom) on the surface increases as the available energy decreases with respect to the adsorption potential well depth. Volatile HF gas, which does not participate in SiO_2 etching under ambient temperature at pressures of several tens of mTorr, can physisorb on the surface at cryogenic temperatures. Once physisorbed layers are activated by energy transfer from incident ions, chemical reactions are triggered, leading to etching.[21,23] With HAR etching generally employing ions with energies of up to several KeV, the activation energy of these chemical reactions is not rate limiting.

The CPE mechanism for SiO_2 involves numerous adsorption probabilities. The reference case probabilities (p_0), corresponding to approximately −70 °C, are listed in Table III. To examine the influence of temperature-dependent adsorption probabilities, these reference values were scaled to lower values (warmer substrate) and higher values (colder substrate). All other parameters that could vary with temperature were held constant to isolate the effect of adsorption probabilities. Etch profiles, obtained by scaling p_0 from 0.03 to 1.25 times the reference value are shown in Fig. 6 for the base-case conditions. As temperature decreases (and adsorption probabilities increase), the etch rate monotonically increases, as enhanced adsorption of H_2O and HF facilitates HF hydrolysis, thereby accelerating the etch process. For this parameterization, the thickness of the water and acid layers was limited to 1 voxel (5 nm thickness). That is, we did not allow condensation, which in the model allows the thickness of water and acid layers to exceed this limit as a thicker physisorbed layer. Since all etch processes, except physical sputtering, are initiated by adsorption in this mechanism, scaling adsorption probabilities to lower values decreases etch rates. Etch rates eventually saturate at lower temperatures as the adsorption probability approaches unity.

Etch rates as a function of adsorption probability for bias powers from 1500 to 3500 W are shown in Fig. 7(a). The etch rates

Published under an exclusive license by the AVS

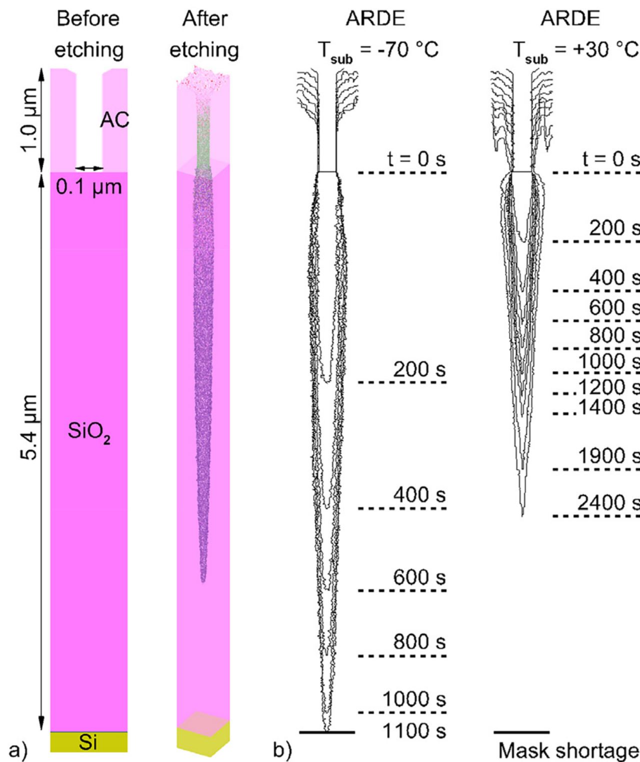

FIG. 5. Feature dimensions and consequences of ARDE. (a) Initial feature geometry of a HAR contact structure consisting of SiO_2, amorphous carbon mask, and Si stopping layer, together with the corresponding 3D profile after etching. (b) Outlines of the feature during etching at different times, demonstrating ARDE at −70°C (cryogenic) and +30°C (ambient) conditions.

are averaged over a fixed period of 600 s. Based solely on adsorption probabilities for the base case, etch rates increase from 193 nm/min for $p = 0.03p_0$ to 404 nm/min for $p = 1.25p_0$, with the etch rate saturating above $p = 0.6p_0$.

In deeper regions of the feature, the re-adsorption of gas-phase H_2O (which is an etch product) continuously sustains the H_2O layer, even under HAR conditions. The surface coverage of the H_2O adsorption layer (including silanol, SiO_2:H_2O, and hydrofluoric acid, SiO_2:H_3O^+:F^-) at the etch front is shown in Fig. 7(b) as a function of etch time. Longer etch times correspond to deeper features and a higher aspect ratio. At the start of etching ($t = 0$ s), no H_2O is present at the etch front in any case, and so etching is largely physical sputtering or activation of dry adsorbed HF. However, as etching proceeds, H_2O is progressively produced as an etch product at the etch front at the bottom of the feature. With Knudsen diffusion of H_2O in the feature,[11,21] H_2O produced deeper in the feature has an increasingly larger probability of adsorbing onto the surface with increasing depth as opposed to diffusing out of the feature. As a result, the surface coverage of H_2O at the etch front increases as etching proceeds (i.e., with increasing time or etch depth). This enhancement is due not only to the

TABLE III. Adsorption probabilities for the base case (T_s = −70°C).

Reaction	Reference probability, p_0
HF–H_2O related reactions	
$H_2O_{(g)} + M_{(s)} \rightarrow H_2O_{(a)} + M_{(s)}$	0.30
$H_2O_{(g,\ a)} + SiO_{2(s)} \rightarrow SiO_2{:}H_2O_{(s)}$	0.80
$H_2O_{(g,\ a)} + SiO_2{:}HF_{(s)} \rightarrow SiO_2{:}H_3O^+{:}F^-_{(s)}$	0.80
$HF_{(g)} + M_{(s)} \rightarrow HF_{(a)} + M_{(s)}$	0.15
$HF_{(g,\ a)} + SiO_{2(s)} \rightarrow SiO_2{:}HF_{(s)}$	0.70
$HF_{(g,\ a)} + SiO_2{:}H_2O_{(s)} \rightarrow SiO_2{:}H_3O^+{:}F^-_{(s)}$	0.80
$H_2O_{(g)} + HF_{(a)} \rightarrow H_3O^+{:}F^-_{(a)}$	0.80
$H_2O_{(a)} + HF_{(g)} \rightarrow H_3O^+{:}F^-_{(a)}$	0.80
Fluorocarbon related reactions[a]	
$CF_{x(g)} + SiO_{2(s)} \rightarrow SiO_2CF_{x(s)}$	0.45–0.89
$CF_{x(g)} + SiO_xC_yF_{z(s)} \rightarrow SiO_xC_yF_{z(s)}$	0.22–0.45
$CF_{x(g)} + SiO_xC_yF_{z(s)} \rightarrow SiO_xC_yF_{z(s)} + Poly_{(s)}$	0.02–0.05

[a] CF_x and SiO_2CF_x include species with x = 1–3. $SiO_xC_yF_z$ denotes SiO_2CF, SiO_2CF_2, SiO_2CF_3, $SiO_2C_2F_3$, $SiO_2C_2F_4$, $SiO_2C_2F_5$, $SiO_2C_2F_6$, and $SiOCF_3$. Poly denotes fluorocarbon polymer formed on the SiO_2 fluorocarbon complex.

higher adsorption probability at lower T_s, but also to the increased likelihood of adsorption for H_2O generated deeper in the feature. The maximum water coverage is about 0.9 for deep features and large adsorption probability. The less than unity coverage results from desorption reactions during the etch process.

With increasing bias power, there is a small increase in reactive fluxes accompanying an increase in ion energy and a narrowing of the angular distribution (more specular scattering). The end result is higher etch rates. The increase in etch rates between 1500 and 3500 W is a factor of 1.5 with the highest adsorption probability (low T_s). The maximum ion energy increases by a factor of 1.45 between 1500 and 3500 W. With a square root energy dependence for chemical sputtering, the increase in energy would account for only a factor of 1.2 in the etch rate. The additional increase can be attributed in part to a larger component of specular scattering due to the narrower angular distribution. The higher etch rate increases production of H_2O deep in the feature, which then enables more adsorption of H_2O to catalyze further reactions.

In addition to HF–H_2O related etch reactions, etching involving CF_x species and physical sputtering occur. These processes are likewise influenced by changes in adsorption probability with temperature. The relative contributions of each etch process can be gauged by tracking specific etch products leaving the feature. For example, CF_x-driven etching produces $CO_{(g)}$ and $CO_{2(g)}$, and physical sputtering produces $SiO_{2(g)}$. At the lowest adsorption probability ($p = 0.03p_0$), the fractional contributions to etching are 60% from HF–H_2O related reactions, 5% from CF_x related reactions, and 35% from physical sputtering. At the highest adsorption probability ($p = 1.25p_0$), the contributions are 88% from HF–H_2O reactions, 6% from CF_x reactions and 6% physical sputtering.

As adsorption probabilities decrease with increasing temperature, surface chemical reactions are suppressed, leading to a larger

13 April 2026 14:38:55

Published under an exclusive license by the AVS

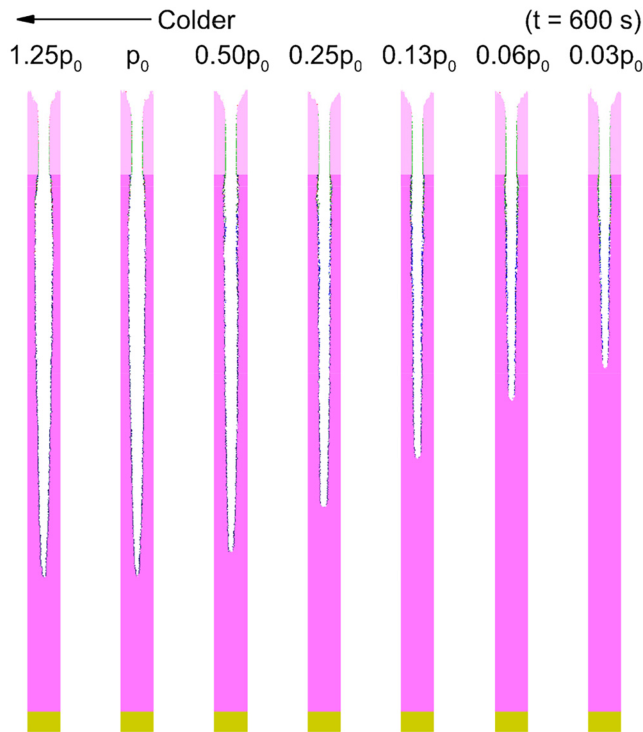

FIG. 6. Etch profiles corresponding to different adsorption probabilities for a bias power of 2500 W. [See Fig. 5(a) for definition of materials and dimensions]. The dark shading lining the feature represents adsorption layers.

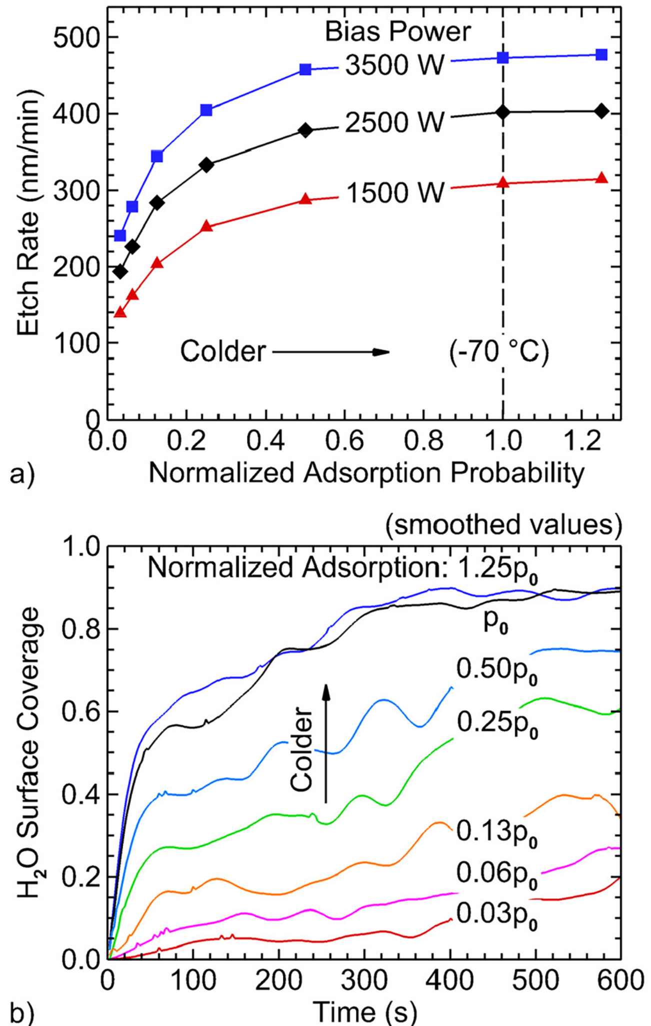

FIG. 7. Process values as a function of adsorption probability. (a) Etch rate as a function of adsorption probability at bias powers of 1500, 2500, and 3500 W. (b) Surface coverage of the H_2O adsorption layer on SiO_2 (including SiO_2:H_2O and SiO_2:H_3O^+:F^-) as a function of time at the etch front for a bias power of 2500 W.

relative contribution to etching by physical sputtering. Conversely, increasing adsorption probabilities at lower temperatures enhance the overall rates of chemical sputtering while decreasing the relative contribution of physical sputtering. The latter is also somewhat decreased by the increase in passivation. Although there is in-feature sputtering of polymer that produces a CF_x product, the majority of CF_x incident onto the etch front originates from the plasma and must diffuse through the feature (one of the origins of ARDE). The contribution of CF_x based processes increases only modestly with decreasing temperature in spite of the increase in adsorption due to these conductance limits on CF_x transport. With H_2O being generated *in situ* near the etch front and being subsequently re-adsorbed, conductance is a less limiting factor. The contribution of HF–H_2O processes therefore increases relative to CF_x processes with decreasing temperature.

B. Condensation

As the substrate temperature decreases, enhanced adsorption of etch precursors leads to an increase in etch rate. However, when the temperature falls below a critical value, condensation occurs, resulting in the formation of thick adsorbed layers. Antoun *et al.*[23] reported that the thickness of the C_4F_8 physisorption continuously increases as the temperature decreases from −112 to −120 °C. Lill *et al.*[21] reported that physisorption allows for multilayer deposition, which in our nomenclature is condensation, and once condensation sets in, an etch stop may occur. Their study reported that at 30 mTorr, condensation temperatures are ≈−49 °C for H_2O, ≈−88 °C for HF, and ≈−196 °C for CF_4. These results imply that, as temperature decreases, condensation of adsorbed H_2O is the first likely to occur among the major incident fluxes. In this regard, Kihara *et al.*[13] observed in etching of SiO_2 in HF-dominated plasmas that the etch rate increased with decreasing temperature until approximately −70 °C, decreasing sharply below that temperature. One interpretation is that the decrease in etch rate was the result of thickening of the adsorption layers due to condensation,

13 April 2026 14:38:55

Published under an exclusive license by the AVS

which then decreased the ability of ions to deliver activation energy to the SiO_2 interface.

In discussions of temperature-dependent etch mechanisms, it is important to note that in CPE reactors, substrate temperature control is typically performed through the ESC and not the wafer itself. The bottom of the wafer is cooled by the ESC and the top surface of the wafer (whose temperature determines reaction probabilities) is heated by incident ion fluxes. As such, the temperature of the top surface of the wafer is typically higher than the ESC setpoint (likely by a few tens of degrees depending on process conditions).[38]

Within the temperature range notionally investigated here (−110 to +30 °C) at 30 mTorr, condensation occurs predominantly in the H_2O adsorbed layer. In this regard, condensation in our model refers to the accumulation of additional H_2O layers on top of the initially adsorbed H_2O and acidified layer on SiO_2. In our base case (−70 °C), condensation was not included. The impact of thickening condensation layers on etch rate was investigated by varying the probability for adsorption of H_2O on top of previously adsorbed H_2O (pure and acidified) from 0 (base case) to $p_c = 0.3$ while keeping other parameters constant. The multilayer condensation probability was implemented in our model, following the Brunauer, Emmett, and Teller (BET) theory in which the initial adsorption and condensation probabilities may differ, however, the probability of multilayer condensation is the same as the first layer.[54] As shown in Fig. 8, increasing condensation probability significantly reduces etch rates, while also increasing roughness on the sidewalls and the etch front due to variation in the thickness of the condensation layer. As with thicker fluorocarbon passivation,[55] thicker condensation layers produce more tapered profiles. Over this range of p_c, the thickness of the adsorption layer at the etch front varies from 0 to an average of 10 nm. Although the intent was to limit thickness to a maximum of 10 nm, statistical variation in surface sites and local morphology will produce occurrences of thicker condensation.

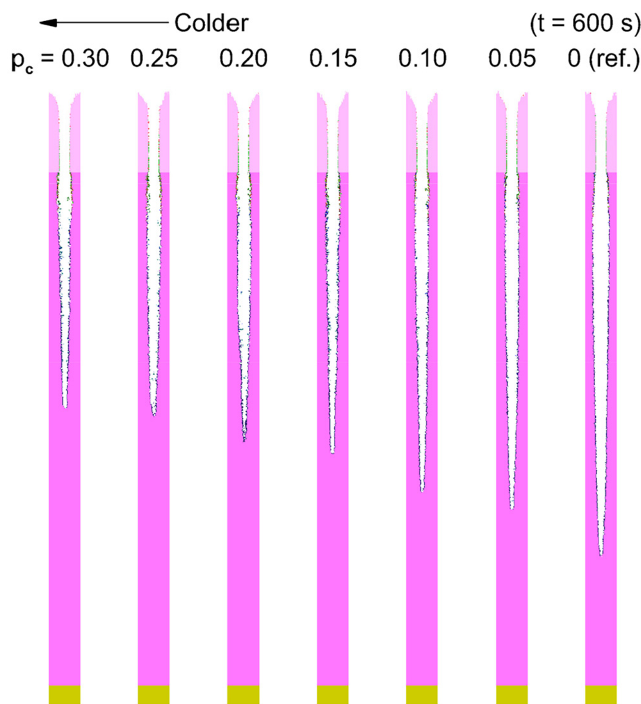

FIG. 8. Etch profiles corresponding to different condensation probabilities (p_c) for a bias power of 2500 W, with the maximum thickness of condensation limited to an average of 10 nm.

With thicker condensation layers, ions must penetrate further through the overlying water to reach the H_2O–SiO_2 interface to transfer energy and activate reactions. Thicker H_2O layers require larger HF fluxes to sustain hydrolysis and surface acidification. Increasing condensation probability from 0 to 0.3 reduced etch rates by approximately 40%.

The effects of condensation, for bias powers of 1500, 2500, and 3500 W, are shown in Fig. 9 for maximum average condensation thickness of 10 and 15 nm while varying p_c from 0 to 0.3. With a maximum average thickness of 10 nm, the etch rate for a bias power of 3500 W decreased by 32% while that for 1500 W decreased by 50%. The higher ion energies produced at 3500 W are able to both better penetrate through the condensation layer and more efficiently thin the condensation layer by sputtering.

With a maximum average condensation thickness of 15 nm, the decrease in etch rates follows the same trends as the thinner condensation layers, though with a more severe decrease in the etch rate. There is more scatter in our results due in large part to the rougher surface with the increase in condensation layer thickness. In our model, after adsorbed H_2O undergoes its initial period of surface diffusion, the voxel representing the condensed H_2O does not move unless sputtered or otherwise chemically reacts. That is, the voxels in the condensed layer do not flow as a fluid. These static voxels lead to roughening (which would be worse in the absence of surface diffusion), while also sputtering less of the condensation layer. In experiments by Cemin *et al.*,[56] thicker H_2O condensation layers on Si were measured with decreasing temperature, exponentially increasing from nominally zero at −100 °C to 12 nm at −150 °C. However, the surface diffusion or flow of the thick H_2O condensation layers has not yet been systematically quantified. Although not conducted in a plasma environment, Thoms *et al.*[57] observed a mobile surface layer during vapor deposition of amorphous solid water (ASW). Their analysis shows that the effective thickness of this mobile layer decreases with decreasing deposition temperature. By analogy, as the temperature decreases, surface diffusion of the condensed H_2O layer is likely to be more limited, even if the total condensed layer becomes thicker.

13 April 2026 14:38:55

C. Etch yield

One of the key parameters in the CPE mechanism contributing to a higher etch rate is the etch yield. Etch yield is the number of atoms (or units of SiO_2) removed from the solid per incident ion (or hot atom/molecule). In the context of the model, the etch yield is the number of SiO_2 voxels removed per incident ion or hot atom (molecule) pseudoparticle. The dependence of the physical sputtering yield of SiO_2 on ion energy has been extensively studied.[58–62] Seah and Nunney[58] recorded that for ion energies as high as 5–10 keV, the Ar^+

Published under an exclusive license by the AVS

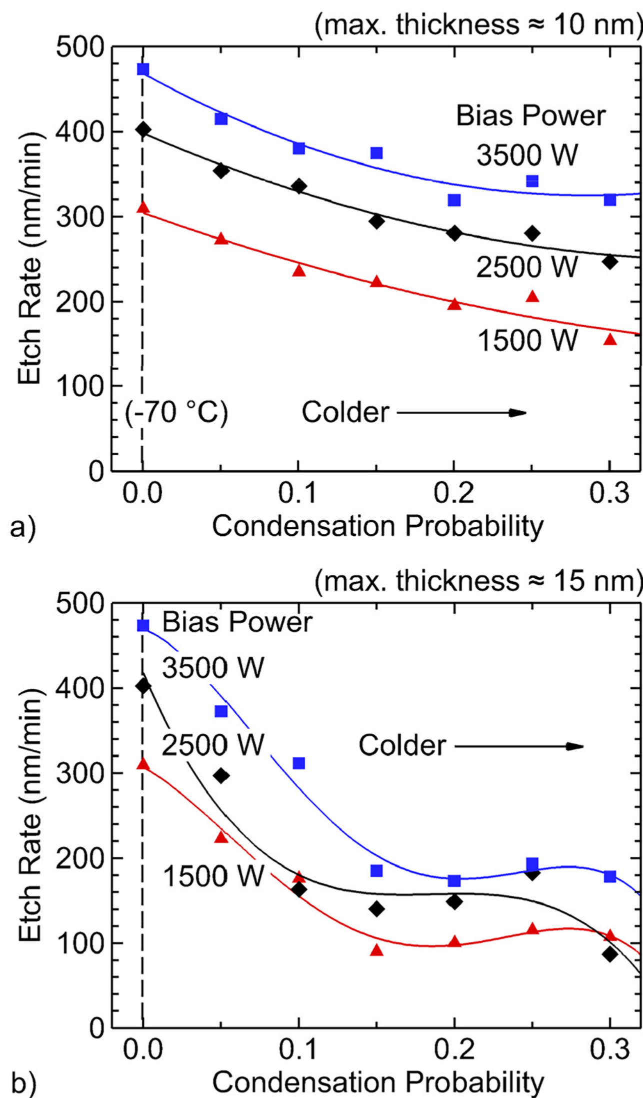

FIG. 9. Etch rate as a function of condensation probability at bias powers of 1500, 2500, and 3500 W, with the maximum average thickness of condensation limited to (a) 10 and (b) 15 nm.

sputtering yield for SiO_2 is only 2–3. Although the etch yield of chemical sputtering in CPE has not yet been quantitatively reported, estimates of the etch yields based on blanket etch rates and incident ion fluxes suggest that the etch yield of CPE is at least two or three times larger than physical sputtering, considering the difference in etch rates. In our model, these higher yields would apply to the fluorinated silanol species (represented as $SiO_2{:}H_3O^+{:}F^-$ in this work), which contains silanol (Si–OH) and fluorinated Si (Si–F).

The threshold energy for physical sputtering of SiO_2 has been reported as 30–50 eV.[60–62] However, in the etching process involving HF and H_2O, the activation barrier for chemical reactions is significantly reduced.[63,64] Hidayat *et al.*[63] demonstrated through density functional theory (DFT) calculations that silanol groups undergo a four-step sequential fluorination by HF, accompanied by OH exchange and H_2O formation, ultimately producing volatile SiF_4 with activation energies of 0.72–0.79 eV per step. These results suggest that the effective threshold energy required for final etching of SiO_2, when fluorinated by HF in the presence of H_2O catalysis, is low, providing a rationale for the enhanced etch yield compared to physical sputtering. The high etch yield of $SiO_2{:}H_3O^+{:}F^-$ may also be attributable to the HF hydrolysis mechanism. HF hydrolysis of SiO_2 surfaces unzips Si–O bonds to form Si–OH and Si–F groups, creating a nanoporous network.[29–31] The nanoporosity of the silanol network and the associated weakened lattice rigidity likely further enhances the yield.

The etch profiles corresponding to varying the etch yield of $SiO_2{:}H_3O^+{:}F^-$ (fluorinated silanol species) and $SiO_2{:}H_2O$ [silanol groups, representing Si–$(OH)_n$ ($n = 1$–3)] with decreasing temperature are shown in Fig. 10(a). In the base case (−70 °C), the etch yields (y_0) were set to 12 molecules/ion for $SiO_2{:}H_3O^+{:}F^-$ and 9 molecules/ion for $SiO_2{:}H_2O$ with a threshold energy of 30 eV. To isolate the effect of etch yield as a function of substrate temperature, etch yields were varied from $0.03y_0$ to $1.25y_0$ while keeping other parameters constant, while operating under the yield limits of the voxel-based yield model discussed in Sec. III. Higher yield conceptually corresponds to lower temperature. The results show that etch depth increases with higher yield with similarity between the $1.25y_0$ and y_0 being due to the yield limit. Consequently, increases in etch rate due to yield changes in y_0 with T_s are likely underestimated here.

The consequences of the effective yield on the etch rate for bias powers of 1500, 2500, and 3500 W are shown in Fig. 10(b). As expected, decreasing temperature and corresponding higher y_0 results in increased etch rates across all bias powers. With bias power increasing from 1500 to 3500 W (a factor of 2.33), the etch rate increases by a factor of 1.6, which aligns with the higher ion energy and increase in ion flux. At the lowest etch yield, removal of SiO_2 is due to physical sputtering and fluorocarbon-based etching.

13 April 2026 14:38:55

D. Specular reflection of scattered particles

When ions scatter from dielectric surfaces such as SiO_2, they generally lose their charge, neutralize (producing hot neutrals), and undergo reflection with both specular and diffusive components. Manson *et al.*[65] reported that when fast particles at keV energies scatter from surfaces at grazing incidence, the energy loss is relatively small. Under HAR etching conditions, energetic ions striking the feature sidewalls before reaching the etch front are likely to impact at grazing angles, undergoing specular reflection while retaining a large fraction of their incident energy.

In HAR etching, ions (or hot neutrals) reaching the etch front consist of particles arriving directly without collisions and particles arriving after undergoing reflection from the sidewalls. The latter population can be influenced by substrate temperature through the sensitivity of scattering probabilities to temperature. At the higher bias voltages that typically produce narrower angular distributions onto the wafer, a larger proportion of ions reach the etch front without scattering from sidewalls.

Published under an exclusive license by the AVS

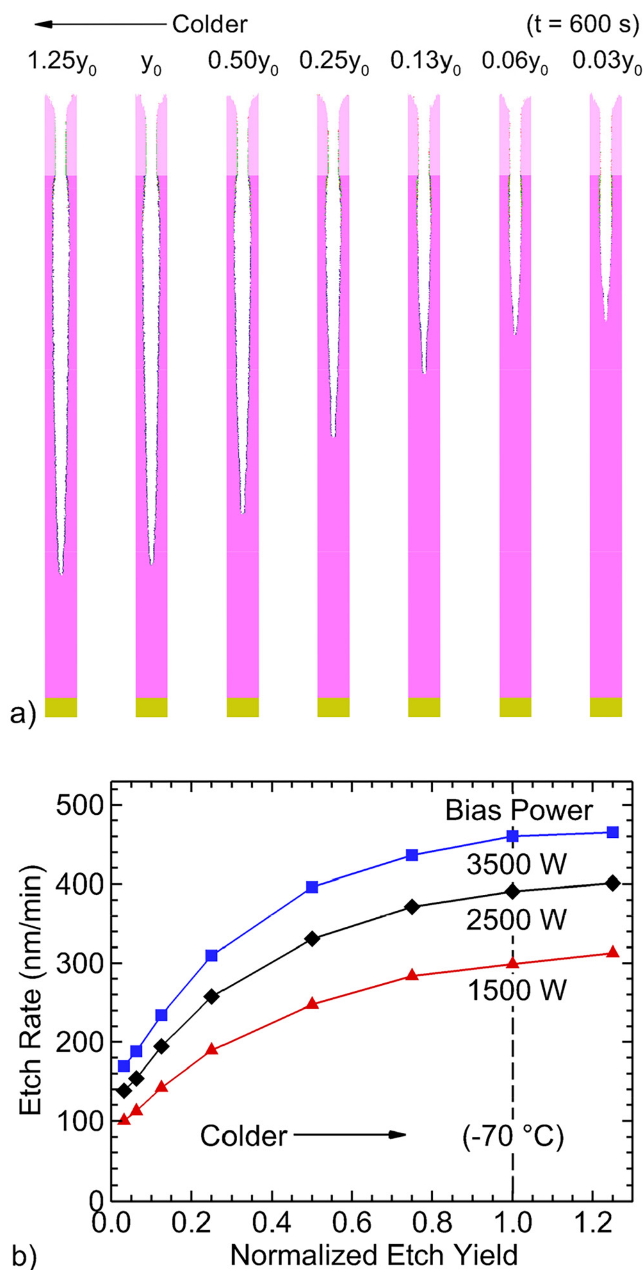

FIG. 10. Etch properties as a function of yield. (a) Etch profiles at a bias power of 2500 W as a function of etch yields of fluorinated silanol (SiO_2:H_3O^+:F^-) and silanol groups (SiO_2:H_2O). (b) Etch rate for a bias power of 1500, 2500, and 3500 W as a function of the etch yield.

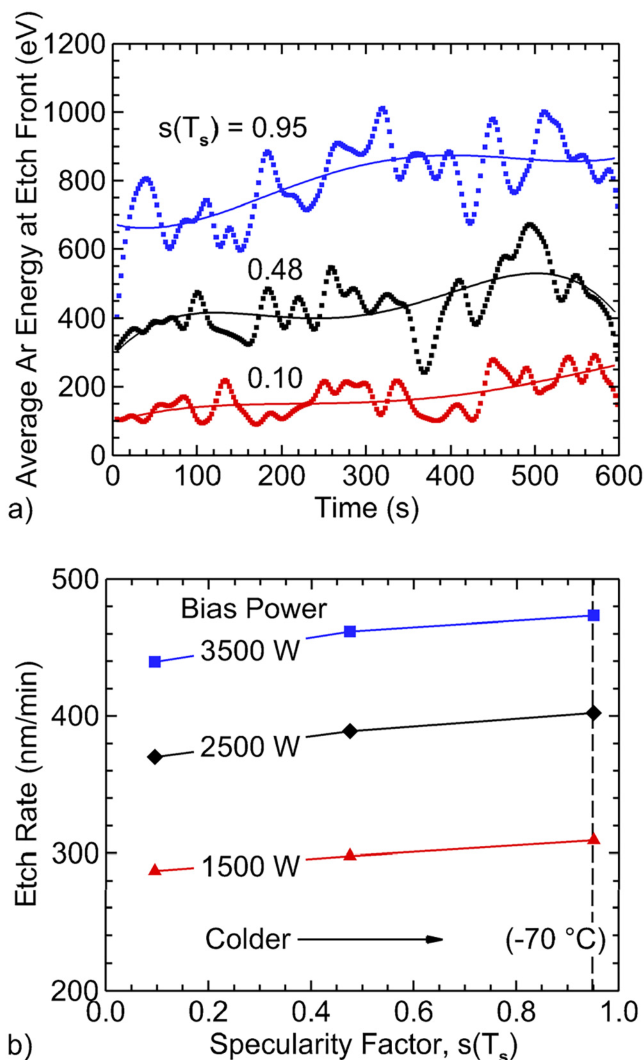

FIG. 11. Etch processes as a function of specularity. (a) Time evolution of the average Ar energy arriving at the etch front, for different values of the temperature-dependent specularity. (b) Etch rate as a function of temperature-dependent specularity at bias powers of 1500, 2500, and 3500 W.

The average energies of Ar hot neutrals (produced after initial reflection of ions from sidewalls) arriving at the etch front as a function of time are shown in Fig. 11(a), for $s(T_s)$ of 0.1, 0.48, and 0.95 corresponding to decreasing T_s. [Recall that increasing $s(T_s)$ increases the specularity of reflection.] Increasing specular reflection supplies higher-energy (hot) atoms to the etch front, which can accelerate the etch rate and mitigate ARDE. Etch rates for bias powers of 1500–3500 W as a function of $s(T)$ are shown in Fig. 11(b). The increase in hot-atom energy with increasing $s(T)$ does produce an increase in the etch rate across all bias powers. However, the increase in etch rate is less than 10% as the majority of the etch is due to the direct incidence of ions. In a tapered feature, a particle reflecting from the sidewall is increasingly likely to undergo a second (or more) reflection, thereby decreasing the hot-atom energy and reducing its yield. We expect a larger contribution of hot atoms to the etch rate, and so a larger influence of $s(T)$ for features that are less tapered.

13 April 2026 14:38:55

Published under an exclusive license by the AVS

E. Redeposition

In conventional HAR etching using carbon-rich fluorocarbon gas mixtures, the etch profile is controlled by passivating the sidewalls with polymer layers. However, in CPE, the high adsorption rate of fluorocarbon radicals promotes the formation of thick polymer layers, which can narrow or clog the feature at the mask or high in the feature. As a result, HF containing plasmas with low carbon content are preferred.[13,14,28] When HF is not directly supplied but instead generated through reactions between a F-donating fluorocarbon and H_2, fluorocarbon-derived passivation will occur. The fluorocarbon-derived passivation is controlled by limiting the mole fraction of the F-donor. In CPE of dielectric materials such as Si_3N_4, the presence of nitrogen enables the formation of nonvolatile passivation layers such as ammonium fluorosilicate,[66] which provides the passivation needed for profile control. By contrast, in HF-dominated plasma etching of SiO_2, no specific passivation layer arising from HF/H_2O reactions has been clearly identified.

Gray *et al.*,[67] reported that during SiO_2 etching, redeposition is dominated by nonvolatile fragments (e.g., SiO_2) formed through physical sputtering while redeposition of volatile by-products, formed through chemical sputtering (e.g., SiF_4), proceeds at a much slower rate. These findings suggest that in CPE of SiO_2 nonvolatile SiO_2 fragments generated by physical sputtering may redeposit and contribute to passivation layer formation.

The representative redeposition reactions are in Table I. $SiO_{2(g)}$ will redeposit on all nonaqueous surfaces. Unlike the initial strongly bonded SiO_2, redeposited SiO_2 has a lower density and weaker bonding, making it more easily removed by ion sputtering. Gas-phase SiO_2 redeposition onto acidified aqueous layers is hydrolyzed forming a passivation layer. In this solution, Si is extracted as SiF_4 and the O as water. The notation $P_{(s)}$ is used here as a generic aqueous passivation serving, in principle, a similar role as polymer deposition in conventional fluorocarbon etching, which is less likely to be sputtered than the original aqueous layer. $P_{(s)}$ is removed by ion (hot atom) sputtering, liberating SiF_4 and leaving behind a nonpassivating aqueous layer.

The redeposition of etch products in HAR must have a small probability, or, once deposited, be rapidly removed. In HAR features, the neutral species convect through Knudsen transport, as their mean free path for collisions with gas-phase species is much longer than the feature width. As a result, etch products produced at the etch front in a feature having an aspect ratio of 40 or 50 requires many hundreds of collisions with sidewalls to leave the feature. A redeposition probability even as small as 0.01 would result in the etch product not leaving the feature. As such, the redeposition probability, p_r, for the base case (−70 °C) is 0.001.

To evaluate the impact of redeposition, all other parameters were held constant, while p_r was varied from 0 to 0.008. The sidewall profiles at 600 s etch time, plotted as height versus CD (width), are shown in Fig. 12(a) for $p_r = 0.001$ and $p_r = 0.008$. At high p_r (0.008), the CD along the feature height reflects a reduction in bowing compared to $p_r = 0.001$. As discussed above, increasing p_r enhances passivation, either through SiO_2 redeposition or the formation of the passivation layer $P_{(s)}$ on the acidified aqueous layer. The top-view comparison of the feature at 4.8 μm, where bowing is most pronounced, shows a smaller feature size for

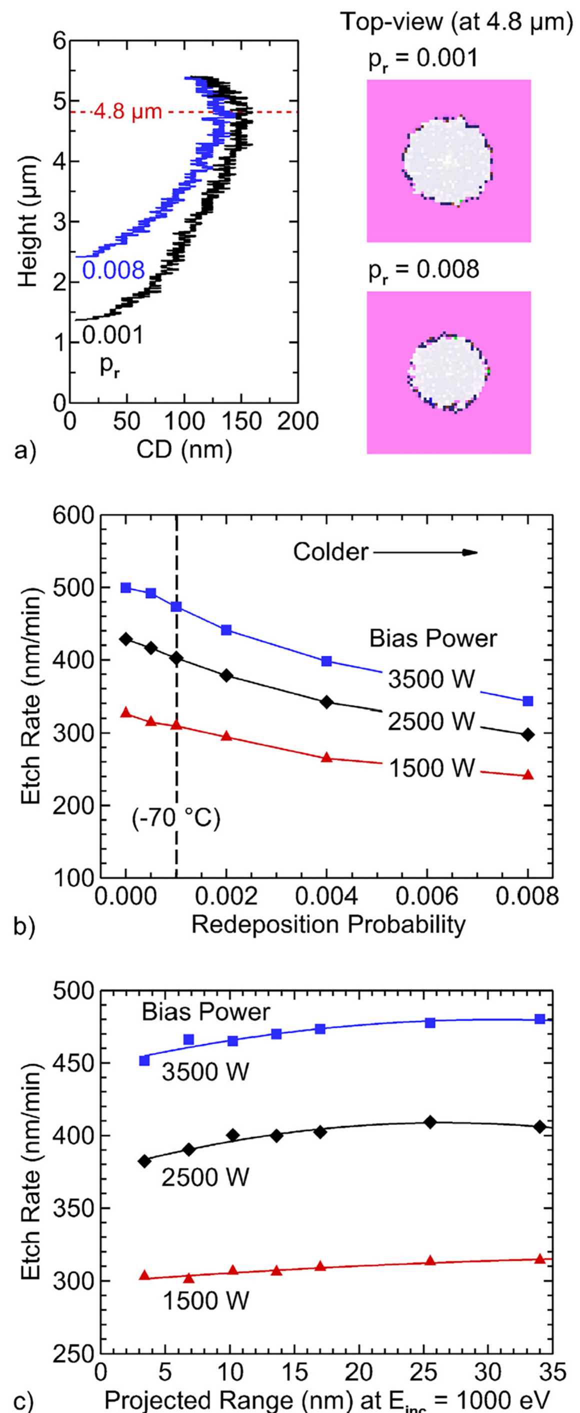

FIG. 12. Feature properties with redeposition probability and implantation range. (a) Feature width (CD) and feature height at 600 s for redeposition probability (p_r) with top-views of profiles at 4.8 μm height, where bowing is most pronounced. Etch rates as a function of (b) redeposition probability and (c) ion implantation range (R_p) at bias powers of 1500, 2500, and 3500 W.

13 April 2026 14:38:55

Published under an exclusive license by the AVS

$p_r = 0.008$. With these small values of p_r, clogging of the feature does not occur as may be seen in fluorocarbon-plasma etching, which has high sticking coefficient radicals. The resulting etch rates for bias powers of 1500–3500 W are shown in Fig. 12(b). For all bias powers, increasing redeposition probability decreases the etch rate (and increases taper) due to the higher rates of passivation. The reduction in the etch rate is more pronounced at higher bias powers. Between $p_r = 0$ and 0.008, the etch rate for 3500 W decreases by 31%, whereas at 1500 W, the decrease is 26%. Only a small fraction of this decrease can be attributed to the narrowing of the feature. At the higher power (and higher ion energies), the proportion of the etching due to physical sputtering is higher, and so there is proportionally more $SiO_{2(g)}$ etch product for redeposition. These results are consistent with experimental reports that increasing bias power (or ion energy) enhances, on a relative basis, physical sputtering, and consequently promotes redeposition.[67,68]

F. Ion (hot atom) penetration through adsorption and condensed layers

In CPE of SiO_2, lowering the substrate temperature leads to the formation of a thick physisorbed layer consisting largely of H_2O together with HF- or CF-containing compounds. Unlike monolayer chemisorption, this multilayer adsorption may reduce transfer of energy from incident ions (hot atoms) to the underlying SiO_2 substrate, thereby decreasing etch rates. One of the key parameters is the range (R_p) of the implanted ion (or atom) through the adsorption or condensation layer. R_p is the distance traveled through the adsorption layer over which the ion deposits its energy. The penetration depth (d_p) is the distance measured normal to the surface at which the ion slows. When ions strike an adsorption layer and implantation occurs, the ion may deposit energy near the surface producing sputtering, produce reactions traversing the adsorption layer, deliver energy to the underlying material, or react with adsorbed species to contribute to the formation of new adsorbed layers. In contrast to parameters described earlier, R_P for ion implantation is not strongly dependent on substrate temperature although the thickness of the adsorption layer will be a function of temperature.

Numerous studies have reported that the R_p of implanted ions increases with incident energy. The penetration depth (d_p) increases as the angle of incidence approaches the normal.[53,69] This suggests that in HAR etching, ions striking the sidewall at grazing angles are less likely to penetrate deeply into the physisorbed H_2O layer than ions striking at normal angles at the etch front. Among ions or hot atoms reaching the etch front, those arriving directly with high energy and near-normal incidence, without sidewall collisions, are expected to have larger d_p than hot atoms scattered from sidewalls, whose energies are lower and arrive at non-normal angles.

To evaluate the influence of R_p on CPE, all other parameters were fixed and R_p was varied in the base case (−70 °C). The parameter sweep was normalized to the R_p of a 1000 eV Ar^+ ion at normal incidence through H_2O, approximately 17 nm. With R_p for SiO_2 being small compared to that for H_2O, once penetrating the water layer, the ions deposit their energy at the surface of SiO_2. As shown in Fig. 12(c), increasing R_p produces higher etch rates as ions are better able to penetrate the physisorbed H_2O layer and deliver energy to the underlying solid to initiate etching reactions. However, the effect is not large, and similar trends occur for all bias powers. For example, the etch rates for a bias power of 1500 W increase by only 4% between $R_p = 3.4$ and 34 nm. For 3500 W, the increase is 6%. With the average adsorption layer for the base case (which does not allow condensation) being ≈5 nm at the etch front and ion energies reaching the etch front at all powers generally exceeding 1 keV, the lower values of R_p already produce d_p commensurate with the adsorption layer thickness. This will not necessarily be the case when condensation produces water layers whose thickness may exceed R_p, thereby significantly reducing the energy delivered to the underlying solid.

G. Neutral transport

Chemically enhanced HAR etching of SiO_2 requires a critical supply of neutrals (including radicals) arriving at the etch front. Neutrals arriving at the wafer surface with isotropic trajectories undergo Knudsen transport deeper into the feature. A low energy particle usually scatters isotropically from the surface (a Lambertian distribution[51]), with, on average, half the particles being directed upward and half downward. This conduction limited transport reduces the flux of neutrals to the etch front, particularly if there is a nonzero sticking coefficient on the walls of the feature.[11,44,70] This reduced transport of etch precursors is a contributor to ARDE in HAR etching.

Transport of anisotropic ions and their specularly reflected hot neutrals to the etch front are less affected by aspect ratio compared to isotropic neutrals. Panagopoulos *et al.*[11] reported that neutral transmission probability decreases sharply with increasing aspect ratio and with smaller feature diameters. They reported that with a zero sticking coefficient, Knudsen transport results in only 1.3% of neutrals reaching the etch front for an aspect ratio of 100. These observations emphasize that surface diffusion of physisorbed neutrals may enhance transport efficiency of neutrals deeper into the feature. Lill *et al.*[21] demonstrated that at low substrate temperatures, higher physisorption probabilities increased surface residence time and rates of diffusion, thereby enhancing neutral transport deeper into the feature.

We examined how increased physisorption probability at low substrate temperatures affects neutral transport, considering both Knudsen transport and surface diffusion. To isolate the consequence of neutral transport from other processes in the mechanism, we began with a pre-etched SiO_2 trench feature, with an opening width of 100 nm, a trench height of 3 μm (aspect ratio = 30), and a depth of 100 nm using periodic boundary conditions. HF molecules were launched into the feature, where upon colliding with sidewalls, they either physisorb or reflect with a Lambertian distribution. The incident flux of HF is that of the base case, $2.4 \times 10^{16}\ cm^{-2}\ s^{-1}$. Adsorbed molecules diffused along the surface for a maximum of 3000 jumps. In this evaluation, the effective surface diffusion coefficient was kept constant, while the physisorption probability was varied.

While varying adsorption probability, the HF flux incident on the bottom of the feature (AR = 30) was measured over a central area of $84 \times 84\ nm^2$. Over the same region, we quantified the

13 April 2026 14:38:55

Published under an exclusive license by the AVS

surface coverage of HF, defined as the fractional area occupied by physisorbed HF. Previous studies have reported that lower physisorption probability (as expected at higher temperature) enhances neutral transport to the bottom of the feature.[11,44,70]

The HF flux and HF surface coverage at the feature bottom as a function of the incident HF fluence (time integral of flux) are shown in Fig. 13 for different adsorption probabilities. The HF flux at the etch front increases as the physisorption probability, p_p, decreases, as expected. At an HF fluence of 2×10^{18} cm^{-2}, the HF flux for $p_p = 0.001$ is 8.9×10^{15} cm^{-2} s^{-1}, whereas for $p_p = 1.0$ the flux is 3.1×10^{14} cm^{-2} s^{-1}, a difference of nearly a factor of 29. The surface coverage at the feature bottom, which more directly governs the effective etch rate, exhibits the opposite trend. The HF surface coverage at the feature bottom increases with increasing p_p. At an HF fluence of 2×10^{18} cm^{-2}, the HF surface coverage is 0.098 for $p_p = 0.001$, and 0.839 for $p_p = 1.0$, a difference of a factor of 9. These results indicate that with high p_p (lower temperature), although a smaller HF flux reaches the etch front, the higher sticking probability results in a larger population of adsorbed HF available to participate in chemical sputtering.

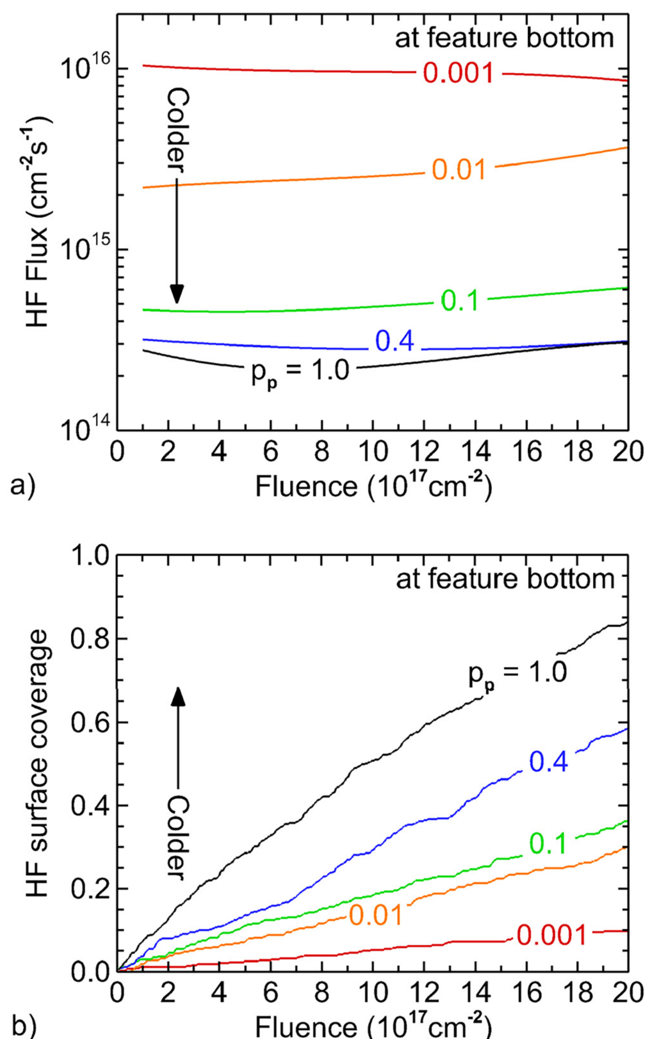

FIG. 13. Fluxes and surface coverage at the bottom of the feature as a function of HF fluence for different physisorption probabilities. (a) HF flux and (b) HF surface coverage.

We found that for these test conditions, diffusion did not have a large effect on surface coverage. When varying the effective diffusion coefficient (number of jumps), the surface coverage at the bottom of the feature only nominally changed. We attribute this result to the lack of reactions that would consume physisorbed species in the test case, which might then be replaced by diffusing species. In the absence of consumption, diffusion both removes and adds adsorbed species at the bottom of the feature. We also found that in full etching cases, as discussed above, surface diffusion did not make large changes in etch rates. We attribute this result to the lack of spontaneous desorption in the model, which would produce sites that might then be repassivated by diffusion.

H. Comprehensive temperature-dependent etch mechanism

The seven mechanistic surface kinetics relevant to cryogenic etching discussed in Secs. IV A–IV G were incorporated into the model with explicit temperature dependences, thereby enabling a comprehensive cryogenic etching simulation. (The range of ion implantation, Sec. IV F, is temperature-independent, with only energy dependence considered.) Given that there is limited temperature-dependent fundamental data, for example, physisorption, condensation, and etch yield, we adopted a hierarchical approach to specify the temperature dependence of these processes. The reference experiments we used to calibrate the model were performed by Kihara *et al.*[13] for SiO_2 etch rates as a function of T_s.

13 April 2026 14:38:55

Adsorption probabilities ($p_a(T_s)$ and $p_{a2}(T_s)$) and redeposition probabilities ($p_r(T_s)$) were modeled using the adsorption rate formalism of Kreuzer *et al.*,[71]

$$p(T_s) = p_0\sqrt{\frac{T_0}{T_s}}\exp(-\alpha(T_s - T_0)), \tag{11}$$

where T_s is the substrate temperature and T_0 is a reference temperature at which each parameter takes on its nominal value, p_0. The parameter α is an empirical coefficient (K^{-1}). Here, $p_a(T_s)$ refers to H_2O–HF related adsorption probability, while $p_{a2}(T_s)$ corresponds to fluorocarbon related adsorption probability, enabling separate treatment of their temperature dependence. The chemical sputtering yield $y(T_s)$ of fluorinated silanol (SiO_2:H_3O^+:F^-) and silanol group (SiO_2:H_2O), and specularity ($s(T_s)$) were similarly modeled using the form

$$f(T_s) = f_0\exp(-\alpha(T_s - T_0)), \tag{12}$$

where T_0 is the reference temperature at which each parameter takes its nominal value, f_0. Both Eqs. (11) and (12) produce a monotonic decrease with increasing temperature.

Published under an exclusive license by the AVS

The condensation of H_2O is assumed to occur below a threshold temperature T_{th}, where the formation of the condensed layer becomes thermodynamically favorable. As the temperature decreases below T_{th}, the condensed layer progressively thickens. At a pressure of 30 mTorr, the H_2O condensation temperature is about −49 °C.[21] Considering that the actual wafer surface temperature is higher than the ESC substrate temperature due to heating,[38] condensation of H_2O was assumed to start from $T_s = -70$ °C in the model. With the condensation probability ($p_c(T_s)$) having a threshold temperature, the form we used is

$$p_c(T_s) = \frac{p_{cm}}{1 + \exp(\alpha(T_s - T_0))}, \quad (13)$$

where p_{cm} is the maximum condensation probability, T_0 is the midpoint temperature at which $p_c(T_s) = p_{cm}/2$, and α determines the steepness of the transition. Here, $T_0 = 186.4$ K, $p_{cm} = 0.58$, and $\alpha = 0.24$. As a result, $p_c(T)$ is small at $T_s = -70$°C, but rapidly increases with decreasing temperature. To better account for the increase in physisorption thickness with decreasing temperature,[23] the maximum average condensation thickness was 15 nm for temperatures below −100 °C.

Model parameters were initially prescribed and then iteratively refined through comparison to experimental data by Kihara *et al.*[13] A summary of the applied temperature dependences is in Table IV.

To evaluate the unified temperature dependence, the etch time was increased from 600 to 1100 s, corresponding to the time required for the fastest etch (−70 °C) to reach the bottom of the feature. Etch profiles after 1100 s for T_s ranging from −110 °C to +30 °C and for a bias power of 2500 W are shown in Fig. 14. Prior to the onset of condensation, the etch rate increases monotonically as the temperature decreases from ambient conditions. At low temperatures, where H_2O condensation occurs, the etch rate drops sharply. The formation of thick H_2O condensed layers acts as an inhibiting barrier within the via, similar to the clogging effect caused by a thick carbon polymer in conventional dielectric etching. These condensed layers hinder ions from delivering sufficient energy to the underlying SiO_2 surface to activate the etch. Thicker H_2O layers would also require higher HF fluxes to become acidified.

The temperature-dependent etch rates, for bias powers of 1500, 2500, and 3500 W, are shown in Fig. 15(a). These etch rates are for partial etches performed for a fixed duration of 1100 s. As expected, the etch rate increases with bias power due to the higher ion energies and fluxes, while the overall temperature dependence is consistent across all bias powers. For example, the etch rate at $T_s = +30$ °C is approximately 40% of that at $T_s = -70$ °C for all powers. We have assumed that T_s is independent of bias power when, in practice, higher bias power would likely translate to a higher wafer surface temperature for a given temperature of the ESC. That said, the decrease in etch rate for all bias powers below $T_s = -70$ °C is attributable to the onset of condensation. The more rapid decrease for 1500 W results from the lower ion energies being less able to penetrate the thicker condensed layers, and so less able to activate the etch. These trends suggest that, although bias power influences the absolute etch rate magnitude, the underlying temperature-dependent surface kinetics are relatively insensitive to bias power. The etching window is then defined by the onset of condensation.

The modeling results show good agreement with the experimental results of Kihara *et al.*, as shown in Fig. 15(b).[13] The model results are an average of the three bias powers. The partial-etch results are for a fixed period of 1100 s. The full-etch results represent over the time at which the etch front reaches the stop layer (Si).

Etch rates as a function of aspect ratio (AR) are shown in Fig. 16. As shown in Fig. 16(a), at $T_s = -70$ °C, the maximum etch rate is approximately 3.7 times higher than that at +30 °C. At $T_s = +30$ °C, the etch rate near an aspect ratio of 20 is about 70 nm/min, whereas at −70 °C, the rate is about 450 nm/min and still above ≈120 nm/min even at an aspect ratio of ≈52. As T_s decreases, the etch rate peaks at progressively larger AR rather than at the beginning of the etch. At high T_s, where adsorption probabilities are small, the etch is dominated by physical sputtering with fluorocarbon enhancements. The fluxes dominating these processes monotonically decrease with AR, and so the etch rate decreases

13 April 2026 14:38:55

TABLE IV. Temperature-dependent model parameters.

Description	T_0 (K)	Nominal value	α	Equation
Adsorption probability $p_a(T_s)$[a]	203.15	p_{a0} (Table III)	0.05	(11)
Adsorption probability $p_{a2}(T_s)$[a]	203.15	p_{a20} (Table III)	0.006[b]	(11)
Redeposition probability $p_r(T_s)$	203.15	$p_{r0} = 0.001$	0.02	(11)
Etch yield $y(T_s)$[c]	203.15	$y_0 = 12$ & 9[d]	0.0347	(12)
Specularity $s(T_s)$[e]	203.15	$s_0 = 0.95$	0.003	(12)
Condensation probability $p_c(T_s)$	186.40	$p_{cm} = 0.58$	0.24	(13)

[a] $p_a(T_s)$ is for H_2O–HF related adsorption and $p_{a2}(T_s)$ is for fluorocarbon related adsorption. Adsorption probabilities at 203.15 K are listed in Table III as p_0.
[b] For the adsorption probabilities of all fluorocarbon species (CF_x), a relatively small value of $\alpha = 0.006$ is applied. Because, unlike HF or H_2O adsorption, which is highly volatile and negligible at room temperature, fluorocarbon adsorption remains sufficiently stable even at room temperature, enabling the etching reaction to proceed.
[c] Chemical sputtering yield of fluorinated silanol (SiO_2:H_3O^+:F^-) or silanol group (SiO_2:H_2O).
[d] y_o of fluorinated silanol is 12 and y_o of silanol group is 9.
[e] $s(T_s)$ represents the degree of specular reflection as a function of temperature.

Published under an exclusive license by the AVS

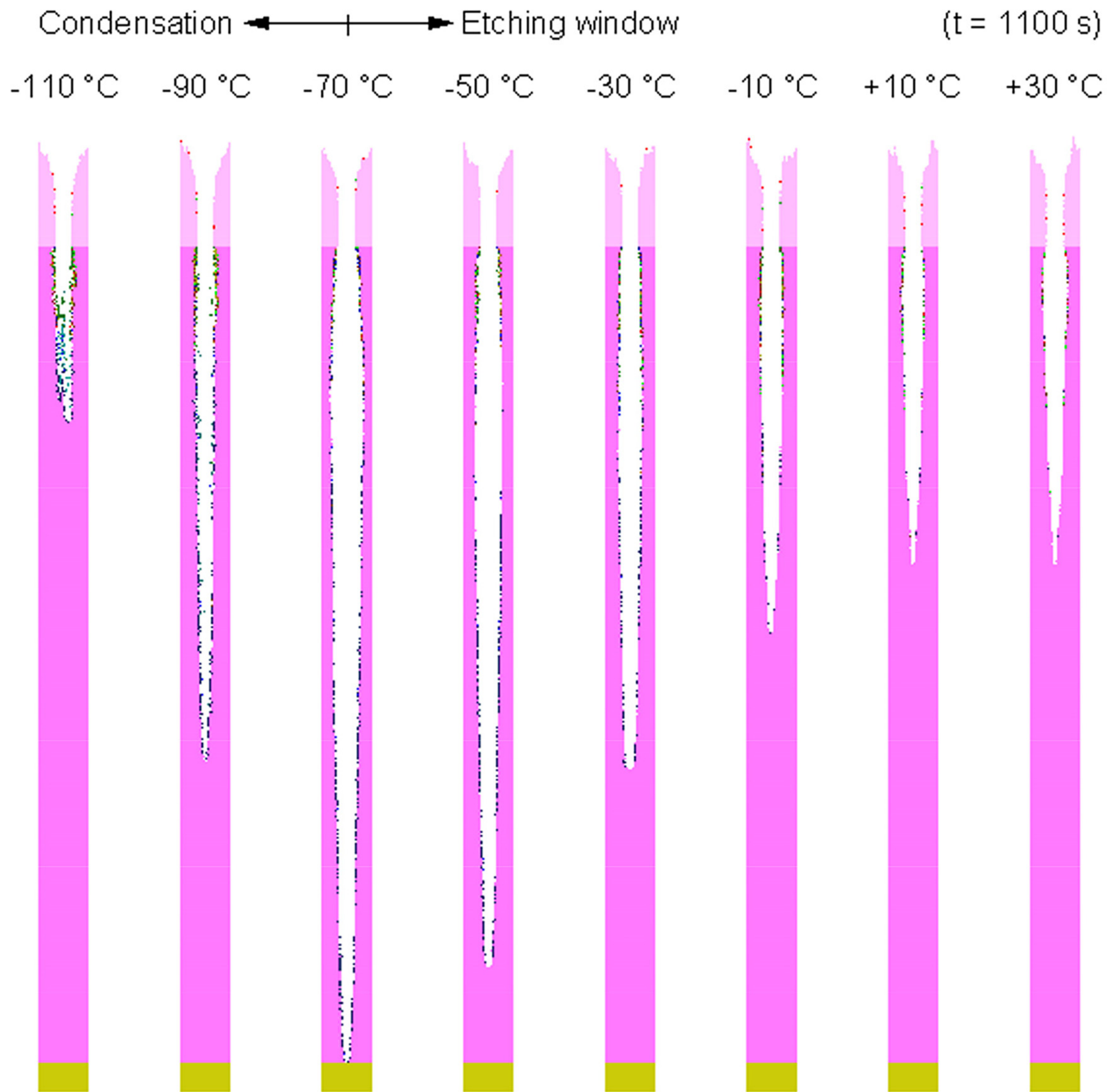

FIG. 14. Etch profiles for different substrate temperatures (T_s) for a bias power of 2500 W. The temperature range before condensation, in which the etch rate increases monotonically with decreasing T_s can be regarded as the etching window.

13 April 2026 14:38:55

(ARDE). At low T_s, H_2O adsorption becomes important, however, the fluxes generated by the $CF_4/H_2/Ar$ gas mixture do not initially contain H_2O. Instead, H_2O is gradually produced through surface reactions during the etch process. As AR increases, the H_2O etch product is progressively trapped in the feature, leading to re-adsorption. At a large enough AR, ion energies and incident HF fluxes to the etch front decrease, and ARDE effects begin to dominate.

The etch rates normalized by the initial etch rate for different T_s are in Fig. 16(b). The aspect ratio at which the etch rate decreases to 50% of its initial value increases with decreasing T_s. At $T_s = +30$ °C, the etch rate falls to 50% of its initial value at AR $\approx$ 11, whereas at -70 °C this occurs at AR $\approx$ 31. These trends suggest that ARDE effects are suppressed at lower substrate temperatures before condensation takes place. This suppression at lower temperatures can be attributed to higher adsorption rates, H_2O regeneration in deeper regions, intrinsically higher etch yields, enhanced specular reflection, and more effective neutral transport.

There are significant changes in profile distortion and mask selectivity as a function of T_s. In high-temperature conventional HAR etching that employs fluorocarbon-rich chemistry, nonuniform fluorocarbon polymer formation can lead to profile distortion

Published under an exclusive license by the AVS

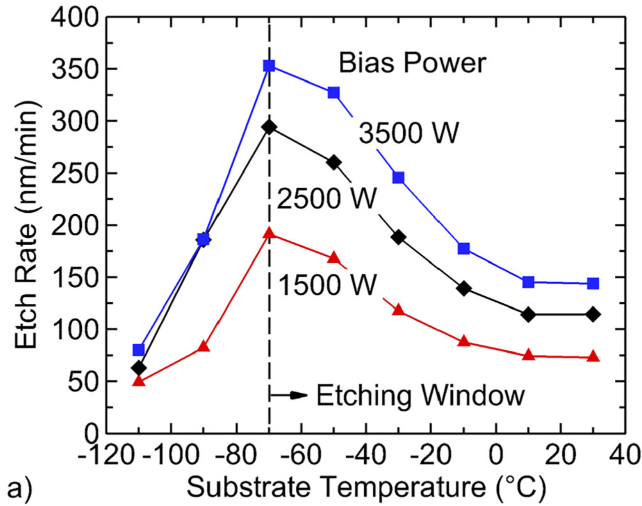

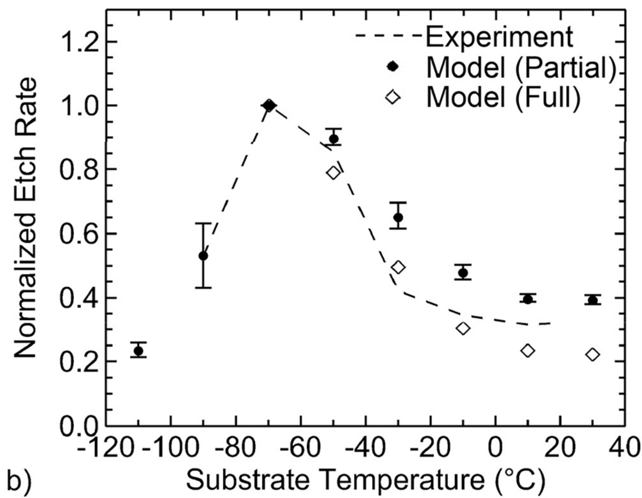

FIG. 15. CPE properties. (a) Model predictions for etch rates as a function of T_s for an etch time of 1100 s and bias powers of 1500, 2500, and 3500 W. (b) Normalized etch rates with respect to the maximum etch rate as a function of T_s, compared to experimental results of Kihara *et al.* (Ref. 13). These results are the average of all powers. The partial-etch results are for a fixed etch time of 1100 s. The full-etch cases correspond to the point at which the etch front reaches the stop layer for a bias of 2500 W.

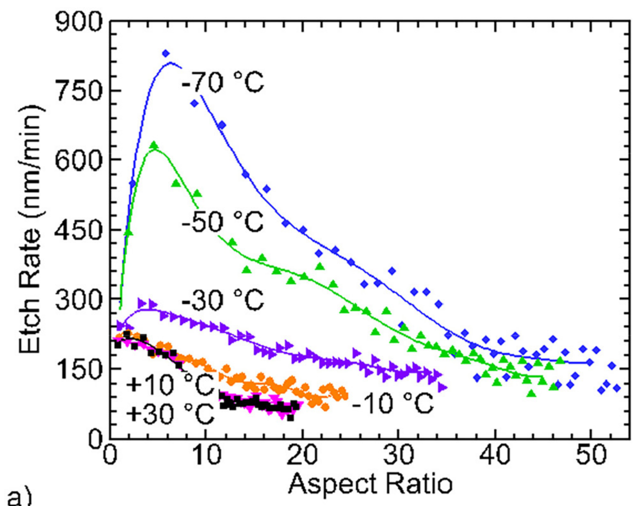

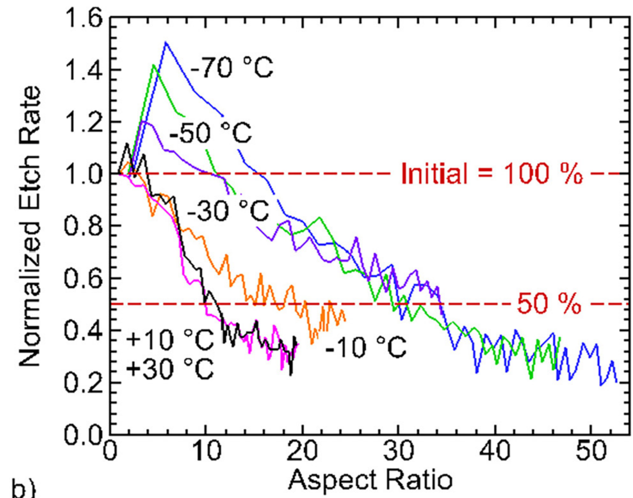

FIG. 16. Etch rates as a function of aspect ratio for different substrate temperatures for a bias of 2500 W, illustrating the ARDE effect. (a) Etch rates. (b) Etch rates normalized by the initial rate.

(e.g., noncircular vias deep in the feature).[4,28] Cryogenic HAR etching based on HF-rich chemistry produces less profile distortion.[28] Although this investigation was conducted in the HF-dominant cryogenic etching regime, temperature variations can still induce noticeable changes in distortion, which are strongly influenced by the masking layer.

Cross-sectional slices of the feature are shown in Fig. 17 for different T_s after the etch reached the stop layer followed by an additional 15% overetch (etching continues for 15% of the time required to reach the stop layer). First, as T_s decreases from −30 to −70 °C, the continuously increasing adsorption rate and proximity to the condensation threshold temperature can lead to a higher likelihood of profile distortion due to nonuniform growth of adsorption layers. Second, as T_s increases from −10 to +30 °C, the top region's distortion becomes increasingly pronounced, leading to severe top bowing. This behavior arises because the etch rate decreases markedly at higher temperatures, resulting in prolonged etch times for HAR features without benefit of passivation to protect sidewalls, which would otherwise reduce bowing. In conventional dielectric etching, this passivation would be provided by CF_x polymer deposition. In the absence of water adsorption, which

13 April 2026 14:38:55

Published under an exclusive license by the AVS

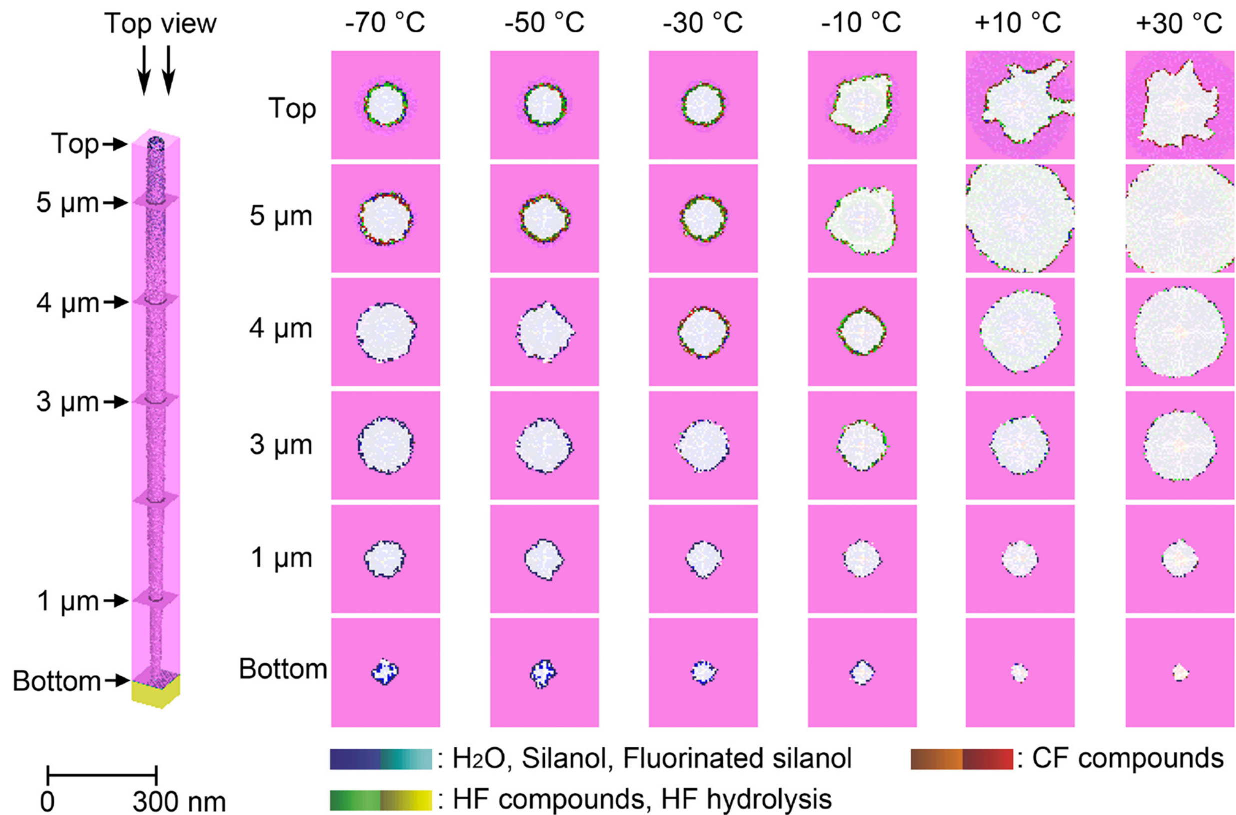

FIG. 17. Top-view images of etched SiO_2 via at different heights (top, 5, 4, 3, 1 μm, and bottom) as a function of substrate temperature for a bias power of 2500 W. A 2 μm-thick erodible amorphous carbon layer was used as the mask. Etching continued until reaching the stop layer, followed by an additional 15% overetch.

13 April 2026 14:38:55

protects the mask, this also enables more mask erosion, which enables ions with a broader angular distribution into the feature.

V. ETCH PROFILE EVOLUTION VERSUS TEMPERATURE

In microelectronics fabrication, profile control, in addition to higher etch rates, is also needed. In the context of HAR plasma etching, profile control refers to the ability to produce features with straight sidewalls with minimum variation in the critical dimension (CD). The CD is usually measured as the width or diameter of the feature. Bowing and tapering are examples of features having less-good profile or CD control. CD control is usually a consequence of controlling the passivation of the sidewalls. Plasma etching of HAR features may take an hour or more,[9,72] which means that the walls in the upper regions of the feature have long exposure to the reactant fluxes. Passivation is typically needed to protect the sidewalls from etching that would produce bowing in the feature. That said, too much passivation can produce tapering.[55] Since mask erosion is known to influence CD control,[4] simulations were performed to isolate the consequences of mask erosion on surface kinetics and CD control. The same feature geometry as in Fig. 5(a) was used having a 100 nm mask opening. However, the original 1 μm AC mask was replaced with a less-erodible (i.e., higher-selectivity) AC hard mask to decouple mask erosion from surface kinetics. For this evaluation, parameters are the same as the base case with the following exceptions. To minimize interference on the substrate between the 2 MHz bias and 40 MHz source, the 40 MHz source power was applied to the top electrode.

Etch profiles for a bias power of 2500 W for T_s between −70 and +30 °C are shown in Fig. 18. Etching continued for a 30% overetch after reaching the stop layer. Sequential snapshots at 350 s intervals show a distinct ARDE effect. As the substrate temperature decreases, the etch rate increases in alignment with our previous discussion.

The bowing CD is the largest diameter of the via. The taper CD is the difference between the bow CD and the diameter at the bottom (generally the minimum CD). Smaller taper CD indicates more vertical profiles. All cryogenic cases (−70, −50, −30 °C) have smaller bowing CD (166, 163, 158 nm, respectively) and taper CD (89, 91, 86 nm) than the ambient temperature case (bowing CD = 180 nm, and taper CD = 124 nm). However, the most vertical and least bowed profiles are not at −70 °C but at −30 °C. These

Published under an exclusive license by the AVS

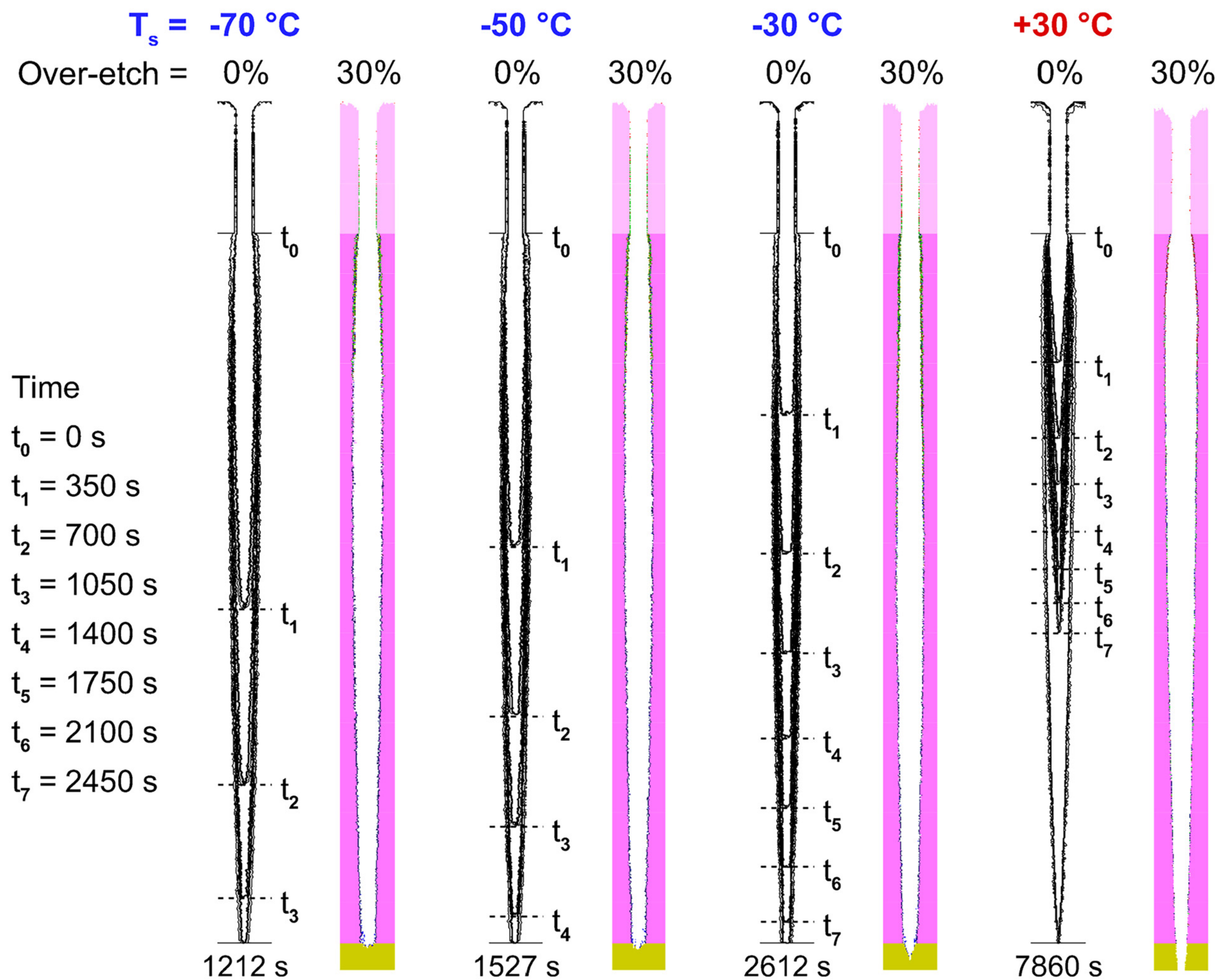

FIG. 18. Full-etch profiles for etched SiO_2 vias for different substrate temperatures for a bias power of 2500 W including a 30% overetch. Sequential snapshots of the etch profiles with an interval of 350 s are shown with snapshot at the time when the etch front reaches the stop layer (0% overetch).

trends indicate that the optimum temperature for CD control is determined by a balance between the lateral etch rate and passivation. For the plasma delivered fluxes for these conditions, the increase in etch rate that occurs when T_s decreases below −30 °C is not sufficiently compensated by passivation, which then produces an increase in bowing. This lack of passivation could also be a result of the water adsorption layers on the sidewalls being too thin or the redeposition of etch product being too small. In the $CF_4/H_2/Ar$ plasma used here, the main etchant HF does not form a strongly nonvolatile passivation layer. Weak passivation arises in this mechanism from redeposition and thickening adsorption layers, however, it is insufficient to minimize bowing and taper CD. In contrast, CPE of Si_3N_4 or ONON structures consisting of alternating SiO_2/Si_3N_4 layers form less-volatile ammonium fluorosilicate (AFS) passivation, which provides stronger sidewall protection, an option not available to CPE of SiO_2.[66]

To demonstrate these trends, additional simulations were performed for the $CF_4/H_2/Ar$ mixture at $T_s = -70$ °C, where the etch rate is the highest. In the base case at $T_s = -70$ °C, the total flux onto the wafer of HF ($\nu = 0$–3) is $2.4 \times 10^{16}\,cm^{-2}\,s^{-1}$, while the CF_3 flux is $3.9 \times 10^{16}\,cm^{-2}\,s^{-1}$, corresponding to a CF_3/HF flux ratio of about 0.17. The passivation flux was artificially increased by increasing the CF_3/HF flux ratio. The resulting etch rates and profiles are shown in Fig. 19. With increasing CF_3 flux, a less bowed profile was produced than at $T_s = -30$ °C (shown in Fig. 18) while retaining a higher etch rate. The bowing CD decreases from 166 nm in the base case at (CF_3/HF = 0.17) to 138 nm for CF_3/HF = 1.0. The taper CD also significantly decreased (from 89 to 69 nm). As expected, the increased passivation leads to a reduction in the etch rate, from 267 to 234 nm/min while still remaining higher than at −30 °C.

13 April 2026 14:38:55

Published under an exclusive license by the AVS

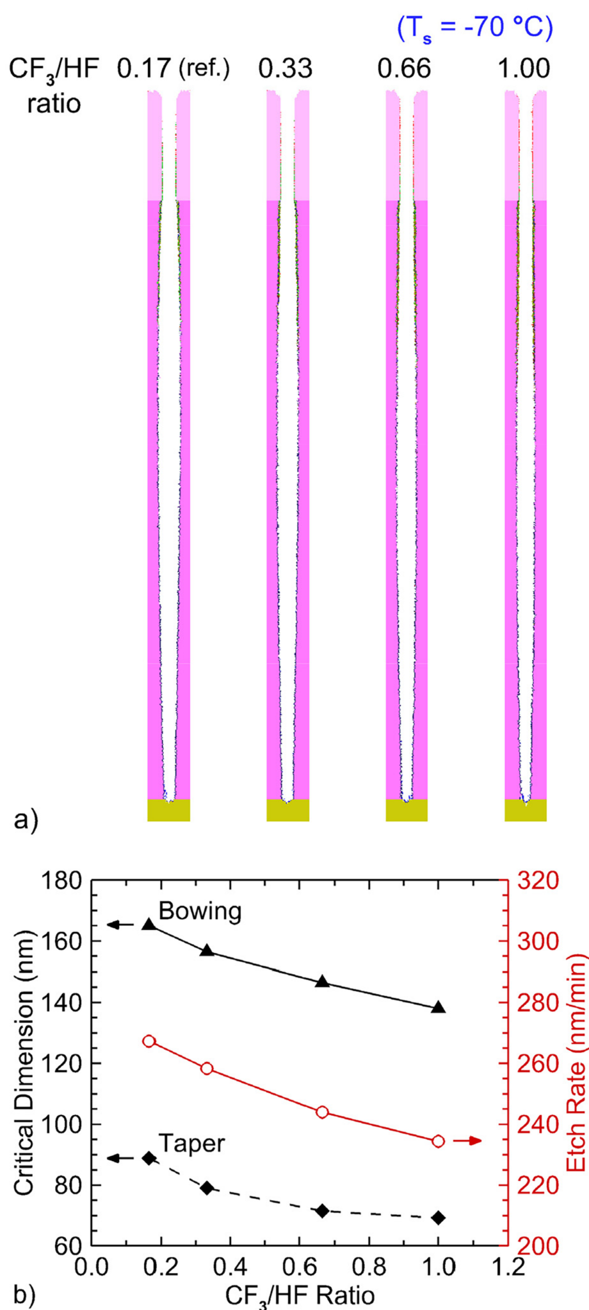

FIG. 19. Comparison of (a) etch profiles and (b) etch characteristics as a function of CF_3/HF flux ratio at T_s = –70 °C and 2500 W for vias in SiO_2. The etch characteristics include the bowing CD, taper CD, and etch rate.

Although CPE is promising for its ability to have higher etch rates than conventional etching, CPE shares the common challenge of profile and CD control with conventional etching.

VI. CONCLUDING REMARKS

This investigation focused on clarifying the mechanisms of CPE of SiO_2. Surface kinetics processes thought to be important in CPE were analyzed, including adsorption, condensation, chemical sputtering yield, specular reflection, neutral transport, redeposition, and ion implantation. The simulations were conducted for a CCP reactor using a $CF_4/H_2/Ar$ mixture at 30 mTorr with a 40 MHz source power of 1000 W and a 2 MHz bias power of 1500–3500 W (nominally, 2500 W), applied to a 3D SiO_2 HAR via-contact structure with an aspect ratio of 54.

At lower temperatures, the increasing adsorption probabilities of HF enable initial dry etching of SiO_2 under ion bombardment, which has H_2O as an etch product. The gas-phase H_2O is re-adsorbed on the surface and plays a pivotal catalytic role. Physisorbed H_2O promotes HF hydrolysis and silanol formation, both of which accelerate surface fluorination and enhance overall reaction rates. Gas-phase H_2O molecules produced at the etch front can re-adsorb locally, allowing sustained catalytic activity even in deep features where neutral transport is limited. When the temperature drops below the H_2O condensation point, increased adsorption leads to the formation of a thick condensed layer, resulting in a decrease in the etch rate. The thick condensation layer reduces the activation energy delivered by ions (hot neutrals), which must penetrate through the layer to reach the underlying SiO_2 interface. The thicker condensation layers require higher HF fluxes to acidify the layer for catalytic activation. Nonuniform condensation can also result in profile distortion.

The enhanced co-adsorption of HF and H_2O not only facilitates faster reaction kinetics but also increases the chemical sputtering yield. The activation energy required to form volatile SiF_4 from fluorinated silanol or silanol groups is as low as ≈0.7–0.8 eV.[63] The co-adsorption promotes HF hydrolysis and facilitates the formation of silanol groups and likely nanoporosity, which likely leads to the higher yields obtained in CPE. At cryogenic temperatures, increased surface rigidity of the lattice also promotes specular reflection, as reduced lattice vibration results in less energy dissipation. This enables hot neutrals to retain higher kinetic energy upon reflection from sidewalls, mildly contributing to etch rate enhancement as they reach the etch front.

While volatile by-products such as SiF_4 from the chemical sputtering are unlikely to redeposit, less-volatile gas-phase SiO_2 generated by physical sputtering likely has increased sticking probabilities at lower temperatures, resulting in minor but non-negligible redeposition layers. Although such redeposition reduces the etch rate, it concurrently protects the sidewall, mitigating bowing and improving verticality.

Neutral transport, consisting of Knudsen transport and surface diffusion, also exhibits temperature-dependent behavior. In general, when the surface has a lower sticking probability (warmer temperatures), neutrals undergo multiple reflections between the sidewalls rather than being adsorbed, allowing them to reach the etch front more rapidly. However, what governs the actual reaction rate is not only the number of neutrals that reach the etch front but those that reach the etch front, are adsorbed, and participate in surface reactions. At lower substrate temperatures, enhanced physisorption facilitates faster buildup of neutral adsorption coverage

13 April 2026 14:38:55

Published under an exclusive license by the AVS

near the etch front and the effect that is enhanced by surface diffusion.

Under conditions where a multilayer condensed film forms, the ion implantation depth becomes critical. Higher ion energy with more normal trajectories are required to penetrate the thicker H_2O physisorbed layer at the etch front to maintain the etch rate.

In summary, the investigation suggests that the higher etch rates and better profile control of CPE likely originate from the synergistic interplay among multiple temperature-dependent surface phenomena—enhanced HF/H_2O co-adsorption, catalytic activation through silanol formation (enhanced etch yield), increased specular reflection, controlled redeposition, and moderated neutral transport. Together, these effects suppress ARDE, accelerate etching, and maintain verticality in HAR features. By carefully tailoring the substrate temperature and gas composition to balance adsorption, condensation, and sputtering dynamics, CPE can be further engineered to achieve both high throughput and precise profile control.

SUPPLEMENTARY MATERIAL

The supplementary material contains a full accounting of the individual reactants, products, and processes encompassing the reaction mechanism discussed in this paper.

ACKNOWLEDGMENT

This work was supported by Samsung Electronics Co., Ltd.

AUTHOR DECLARATIONS

Conflict of Interest

The authors have no conflicts to disclose.

Author Contributions

Yeon Geun Yook: Conceptualization (equal); Formal analysis (lead); Investigation (lead); Methodology (lead); Software (lead); Validation (lead); Visualization (lead); Writing – original draft (lead); Writing – review & editing (equal). **Hyunjae Lee:** Conceptualization (equal); Funding acquisition (equal); Project administration (equal); Resources (equal); Supervision (equal); Writing – review & editing (equal). **Sang Ki Nam:** Conceptualization (equal); Funding acquisition (equal); Project administration (equal); Supervision (equal); Writing – review & editing (equal). **Mark J. Kushner:** Conceptualization (equal); Funding acquisition (lead); Investigation (equal); Methodology (equal); Project administration (equal); Supervision (equal); Writing – review & editing (equal).

DATA AVAILABILITY

The data that support the findings of this study are available within the article or are available from the corresponding author upon reasonable request.

REFERENCES

[1]V. M. Donnelly and A. Kornblit, J. Vac. Sci. Technol. A **31**, 50825 (2013).
[2]I. Adamovich *et al.*, J. Phys. D: Appl. Phys. **55**, 373001 (2022).
[3]K. Ishikawa, K. Karahashi, T. Ishijima, S. Il Cho, S. Elliott, D. Hausmann, D. Mocuta, A. Wilson, and K. Kinoshita, Jpn. J. Appl. Phys. **57**, 06JA01 (2018).
[4]M. Miyake, N. Negishi, M. Izawa, K. Yokogawa, M. Oyama, and T. Kanekiyo, Jpn. J. Appl. Phys. **48**, 08HE01 (2009).
[5]J.-K. Lee, I.-Y. Jang, S.-H. Lee, C.-K. Kim, and S. H. Moon, J. Electrochem. Soc. **157**, D142 (2010).
[6]M. Wang and M. J. Kushner, J. Appl. Phys. **107**, 23309 (2010).
[7]G. S. Oehrlein *et al.*, J. Vac. Sci. Technol. B **42**, 41501 (2024).
[8]R. Micheloni, L. Crippa, C. Zambelli, and P. Olivo, Computers **6**, 27 (2017).
[9]B. Wu, A. Kumar, and S. Pamarthy, J. Appl. Phys. **108**, 51101 (2010).
[10]W. Jeong *et al.*, Materials **16**, 3820 (2023).
[11]T. Panagopoulos and T. Lill, J. Vac. Sci. Technol. A **41**, 33006 (2023).
[12]J. W. Coburn and H. F. Winters, Appl. Phys. Lett. **55**, 2730 (1989).
[13]Y. Kihara, M. Tomura, W. Sakamoto, M. Honda, and M. Kojima, "Beyond 10 μm depth ultra-high speed etch process with 84% lower carbon footprint for memory channel hole of 3D NAND flash over 400 layers," in *2023 IEEE Symposium on VLSI Technology and Circuits*, Kyoto, Japan, June 11–16 (IEEE, NY, 2023), pp. 1–2.
[14]T. Lill *et al.*, J. Vac. Sci. Technol. A **42**, 63006 (2024).
[15]S. Tachi, K. Tsujimoto, and S. Okudaira, Appl. Phys. Lett. **52**, 616 (1988).
[16]J. W. Bartha, J. Greschner, M. Puech, and P. Maquin, Microelectron. Eng. **27**, 453 (1995).
[17]X. Mellhaoui, R. Dussart, T. Tillocher, P. Lefaucheux, P. Ranson, M. Boufnichel, and L. J. Overzet, J. Appl. Phys. **98**, 104901 (2005).
[18]T. Tillocher, R. Dussart, X. Mellhaoui, P. Lefaucheux, N. Mekkakia Maaza, P. Ranson, M. Boufnichel, and L. J. Overzet, J. Vac. Sci. Technol. A **24**, 1073 (2006).
[19]R. Dussart, R. Ettouri, J. Nos, G. Antoun, T. Tillocher, and P. Lefaucheux, J. Appl. Phys. **133**, 113306 (2023).
[20]S. Tinck, E. C. Neyts, and A. Bogaerts, J. Phys. Chem. C **118**, 30315 (2014).
[21]T. Lill, I. L. Berry, M. Shen, J. Hoang, A. Fischer, T. Panagopoulos, J. P. Chang, and V. Vahedi, J. Vac. Sci. Technol. A **41**, 23005 (2023).
[22]J. Nos, S. Iséni, M. Kogelschatz, G. Cunge, P. Lefaucheux, R. Dussart, T. Tillocher, and É. Despiau-Pujo, Appl. Phys. Lett. **126**, 31602 (2025).
[23]G. Antoun, T. Tillocher, P. Lefaucheux, J. Faguet, K. Maekawa, and R. Dussart, Sci. Rep. **11**, 357 (2021).
[24]T. Ohiwa, K. Horioka, T. Arikado, I. Hasegawa, and H. Okano, Jpn. J. Appl. Phys. **31**, 405 (1992).
[25]G. Antoun *et al.*, Jpn. J. Appl. Phys. **58**, SEEB03 (2019).
[26]M. Hori, Rev. Mod. Plasma Phys. **6**, 36 (2022).
[27]S. Rauf and A. Balakrishna, J. Vac. Sci. Technol. A **35**, 021308 (2017).
[28]M. Shen *et al.*, Jpn. J. Appl. Phys. **62**, SI0801 (2023).
[29]S. N. Hsiao *et al.*, Small Methods **8**, 2400090 (2024).
[30]C. R. Helms and B. E. Deal, J. Vac. Sci. Technol. A **10**, 806 (1992).
[31]D. M. Knotter, J. Am. Chem. Soc. **122**, 4345 (2000).
[32]Y. Ono, S. Nagai, Y. Hayashi, S. Urashima, and H. Yui, J. Am. Ceram. Soc. **106**, 4052 (2023).
[33]S. N. Hsiao, M. Sekine, K. Ishikawa, Y. Iijima, Y. Ohya, and M. Hori, Appl. Phys. Lett. **123**, 212106 (2023).
[34]M. J. Kushner, J. Phys. D: Appl. Phys. **42**, 194013 (2009).
[35]S. H. Song and M. J. Kushner, Plasma Sources Sci. Technol. **21**, 055028 (2012).
[36]Y. Zhang, M. J. Kushner, N. Moore, P. Pribyl, and W. Gekelman, J. Vac. Sci. Technol. A **31**, 061311 (2013).
[37]Y. Yang, M. Strobel, S. Kirk, and M. J. Kushner, Plasma Processes Polym. **7**, 123 (2010).
[38]S. Il Cho, H. K. Park, S. An, and S. J. Hong, Appl. Sci. **13**, 9533 (2023).
[39]A. V. Vasenkov, X. Li, G. S. Oehrlein, and M. J. Kushner, J. Vac. Sci. Technol. A **22**, 511 (2004).
[40]A. V. Vasenkov and M. J. Kushner, J. Appl. Phys. **95**, 834 (2004).
[41]V. Volynets, Y. Barsukov, G. Kim, J.-E. Jung, S. K. Nam, K. Han, S. Huang, and M. J. Kushner, J. Vac. Sci. Technol. A **38**, 023007 (2020).
[42]G. C. Manke and G. D. Hager, J. Phys. Chem. Ref. Data **30**, 713 (2001).

13 April 2026 14:38:55

Published under an exclusive license by the AVS

[43]M. Cizek, J. Horácek, M. Allan, I. I. Fabrikant, and W. Domcke, J. Phys. B: At., Mol. Opt. Phys. **36**, 2837 (2003).
[44]S. Huang, C. Huard, S. Shim, S. K. Nam, I.-C. Song, S. Lu, and M. J. Kushner, J. Vac. Sci. Technol. A **37**, 31304 (2019).
[45]Y. Zhang, C. Huard, S. Sriraman, J. Belen, A. Paterson, and M. J. Kushner, J. Vac. Sci. Technol. A **35**, 21303 (2017).
[46]C. M. Huard, S. Sriraman, A. Paterson, and M. J. Kushner, J. Vac. Sci. Technol. A **36**, 06B101 (2018).
[47]Y. Barsukov, M. Wang, Q. Xu, and T. Lill, "Quantum chemistry and integrated modeling for understanding the mechanisms of selective and cryogenic atomic-scale etching," in *AVS 71st International Symposium and Exhibition*, Charlotte, NC, USA, September 21–26 (AVS, NY, 2025).
[48]D. M. Goodstein, C. A. Dirubio, B. H. Cooper, and K. Burke, Surf. Rev. Lett. **01**, 175 (1994).
[49]C. A. DiRubio, D. M. Goodstein, B. H. Cooper, and K. Burke, Phys. Rev. Lett. **73**, 2768 (1994).
[50]J. Powers, J. R. Manson, C. E. Sosolik, J. R. Hampton, A. C. Lavery, and B. H. Cooper, Phys. Rev. B **70**, 115413 (2004).
[51]J. H. Lambert, *Photometria Sive de Mensura et Gradibus Luminis, Colorum et Umbrae* (Klett, Augsburg, 1760).
[52]B. T. Phong, Commun. ACM **18**, 311 (1975).
[53]J. F. Ziegler, M. D. Ziegler, and J. P. Biersack, Nucl. Instrum. Methods Phys. Res. Sect. B **268**, 1818 (2010).
[54]S. Brunauer, P. H. Emmett, and E. Teller, J. Am. Chem. Soc. **60**, 309 (1938).
[55]S. Samukawa and T. Mukai, J. Vac. Sci. Technol. B **18**, 166 (2000).
[56]F. Cemin, A. Girard, and C. Cardinaud, Appl. Surf. Sci. **637**, 157941 (2023).
[57]E. Thoms, J. P. Gabriel, and R. Richert, Phys. Rev. Lett. **135**, 028001 (2025).
[58]M. P. Seah and T. S. Nunney, J. Phys. D: Appl. Phys. **43**, 253001 (2010).
[59]K. Karahashi, K.-i. Yanai, K. Ishikawa, H. Tsuboi, K. Kurihara, and M. Nakamura, J. Vac. Sci. Technol. A **22**, 1166 (2004).
[60]T. Faraz, Y. G. P. Verstappen, M. A. Verheijen, N. J. Chittock, J. E. Lopez, E. Heijdra, W. J. H. Van Gennip, W. M. M. Kessels, and A. J. M. MacKus, J. Appl. Phys. **128**, 213301 (2020).
[61]D. V. Lopaev, T. V. Rakhimova, A. T. Rakhimov, A. I. Zotovich, S. M. Zyryanov, and M. R. Baklanov, J. Phys. D: Appl. Phys. **51**, 02LT02 (2018).
[62]D. R. Shibanov, D. V. Lopaev, K. I. Maslakov, M. R. Konnikova, and A. T. Rakhimov, Vacuum **231**, 113767 (2025).
[63]R. Hidayat, H. L. Kim, K. Khumaini, T. Chowdhury, T. R. Mayangsari, B. Cho, S. Park, and W. J. Lee, Phys. Chem. Chem. Phys. **25**, 3890 (2023).
[64]J. K. Kang and C. B. Musgrave, J. Chem. Phys. **116**, 275 (2002).
[65]J. R. Manson and R. H. Ritchie, Phys. Rev. B **49**, 4881 (1994).
[66]S. N. Hsiao, M. Sekine, Y. Iijima, and M. Hori, Chem. Mater. **36**, 11042 (2024).
[67]D. C. Gray, V. Mohindra, and H. H. Sawin, J. Vac. Sci. Technol. A **12**, 354 (1994).
[68]J.-H. Min, S.-W. Hwang, G.-R. Lee, and S. Heup Moon, J. Vac. Sci. Technol. B **21**, 1203 (2003).
[69]Y. Kido and J. Kawamoto, J. Appl. Phys. **58**, 3377 (1985).
[70]T. Tsutsumi, T. Kurushima, M. Sekine, M. Hori, and K. Ishikawa, "Transport mechanism of active species in high-aspect-ratio hole during plasma etching," in *9th Asia-Pacific Conference on Plasma Physics*, Fukuoka, Japan, September 21–26 (AAPPS-DPP, Japan, 2025).
[71]H. J. Kreuzer and Z. W. Gortel, *Physisorption Kinetics* (Springer, Berlin, 1986), p. 12.
[72]M. Pedersen and M. Huff, J. Microelectromech. Syst. **26**, 448 (2017).

13 April 2026 14:38:55

Published under an exclusive license by the AVS